Chapter 5

Neutron induced reaction cross section measurement for zirconium (Zr), niobium (Nb), strontium (Sr) and rubidium (Rb) isotopes up to the energy of 20 MeV

5.1 Introduction

In this chapter, the neutron induced reactions cross section for ^{90}Zr [1], ^{93}Nb, ^{88}Sr [2] and ^{85}Rb [3] isotopes have been presented in the energy range 10 to 20 MeV. The reaction cross section was determined using the neutron activation analysis and offline γ-ray spectroscopy method. The reaction cross section of the reference monitor ^{115}In(n,n')^{115m}In was utilized for the cross section measurements of ^{90}Zr isotope, whereas the reaction cross section of the reference monitor ^{27}Al(n,α)^{24}Na was used for the measurements of ^{93}Nb, ^{88}Sr, and ^{85}Rb isotopes. The neutrons of desired energies were produced via ^{7}Li(p,n)^{7}Be reaction [4, 5]. The covariance analysis was used to perform detailed uncertainty propagation in the measurements [6]. The reaction cross sections were reported with their uncertainties, covariance and correlation matrix. The corrections for γ-ray coincidence, γ-ray self-attenuation and low energy background corrections were made in the cross section calculations. The comparison of measured (n,2n) and (n,p) reaction cross sections of ^{90}Zr, ^{93}Nb, ^{88}Sr and ^{85}Rb was done with the available cross section data in EXFOR data base [7]. Theoretical calculations were carried out using TALYS 1.9 [8] and EMPIRE 3.2 [9] codes in the neutron energy range from threshold to 20 MeV. The measured cross section of ^{90}Zr(n,2n)^{89}Zr and ^{90}Zr(n,p)^{90m}Y reactions was compared with the evaluated data from ENDF/B-VIII.0 [10], JENDL-4 [11], JEFF-3.3 [12] and ROSFOND-2010 [13]. The measured cross section of ^{93}Nb(n,2n)^{92m}Nb and ^{88}Sr(n,2n)^{87m}Sr reactions was compared with the JENDL/AD-2017 [14], TENDL-2019 [15] and JEFF-3.3 [12] evaluated data. The measured cross section of ^{85}Rb(n,p)^{85m}Kr and ^{85}Rb(n,2n)^{84m}Rb reactions was compared with the JENDL-5 [16] and EAF-2010 [17] evaluated data.

This chapter is divided into five sections from 5.2 to 5.6. The experimental details are given in Section 5.2. The cross section measurements with comprehensive covariance analysis for ^{90}Zr(n,2n)^{89}Zr and ^{90}Zr(n,p)^{90m}Y reactions are described in Section 5.3. The cross section measurements using covariance analysis for the reactions ^{93}Nb(n,2n)^{92m}Nb and ^{88}Sr(n,2n)^{87m}Sr are described in Section 5.4. The cross section measurements for the reactions ^{85}Rb(n,p)^{85m}Kr and ^{85}Rb(n,2n)^{84m}Rb, together with a thorough covariance analysis, are described in Section 5.5. The conclusion of the present experiment is covered in Section 5.6.

5.2 Experimental Details

The experiment was carried out at 6 meter 14UD BARC-TIFR Pelletron facility, Mumbai-India which is the accelerator based particle neutron source[2] [18]. Through the $p + {}^{7}Li \rightarrow n + {}^{7}Be$ process, proton beams with energy ranging from 10 to 22 MeV were accelerated and bombarded into naturally occurring Li-foil to generate neutron beams. The Li-foil thickness was 8 mg/cm^2, positioned between two tantalum (Ta) foils with a thickness of ~ 4 mg/cm^2 on the front side and a 0.1 mm thick foil on the back side. Using SRIM software, the proton energy degradation through Li-foil was determined to be 80-90 keV [19]. *Figure 5.1* displays a schematic diagram of the present experiment. The Ta-Li-Ta stack was kept 2.1 cm away from the target samples with the monitor at 0° with respect to the proton beam direction. The proton beam current was monitored and recorded at a time interval during irradiation. The details of the experiments performed in the TIFR-BARC Pelletron facility for different target and monitor samples are given in *Table 5.1*.

---

[2] A brief summary about Neutron source is given in Section 2.2.

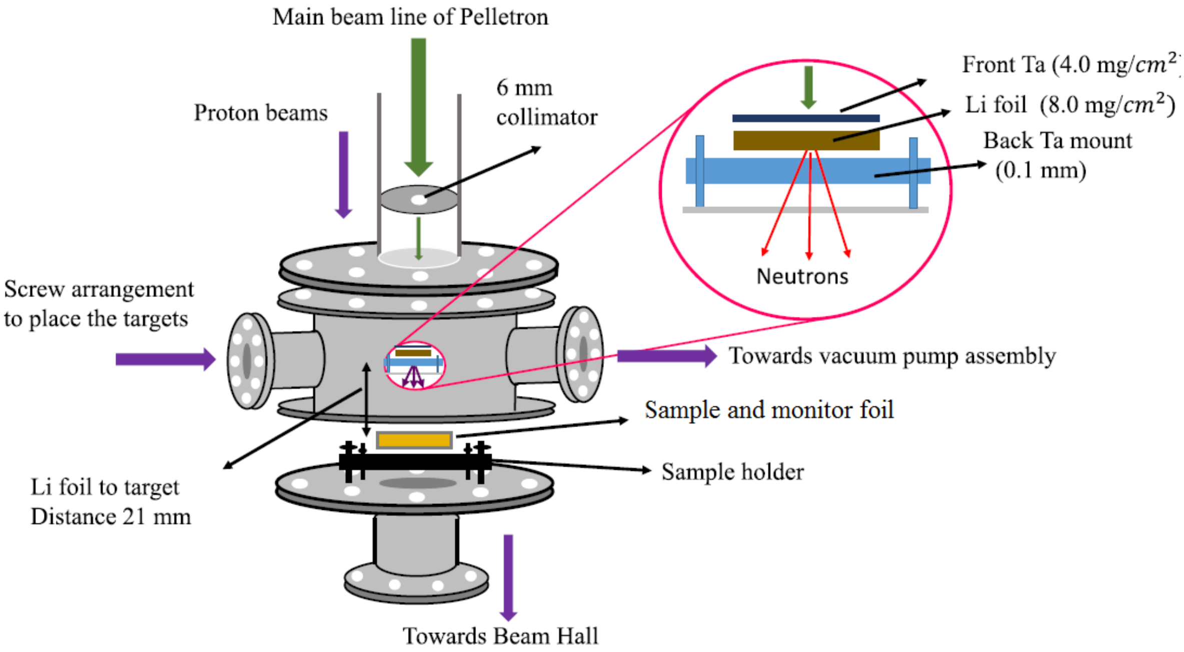

Figure 5.1 A schematic diagram of experimental set up for irradiation [20]

Table 5.1 Details of present experiments

Experiments details	Set I	Set II	Set III
Proton energies (MeV)	13, 16, 19, 22	16, 19, 22	15, 18, 19, 21
Neutron energies (MeV)	10.95, 13.97, 16.99, 20.02	13.97, 16.99, 20.02	12.97, 15.72, 16.73, 18.99
Sample reaction	^{90}Zr(n,2n)^{89}Zr, ^{90}Zr(n,p)^{90m}Y	^{93}Nb(n,2n)^{92m}Nb, ^{88}Sr(n,2n)^{87m}Sr	^{85}Rb(n,2n)^{84m}Rb, ^{85}Rb(n,p)^{85m}Kr
Monitor reaction	^{115}In(n,n’)^{115m}In, ^{27}Al(n,α)^{24}Na	^{27}Al(n,α)^{24}Na	^{27}Al(n,α)^{24}Na

In the experiments, the energetic proton beams incident on the Li target. The threshold energy of $^{7}Li(p,n)^{7}Be$ reaction with the ground state ^{7}Be is 1.881 MeV, whereas for the first excited state, it is 2.37 MeV. Therefore there is a contribution from a second group of neutrons from the $^{7}Li(p,n)^{7}Be$ reaction above 2.37 MeV proton energy. Above the proton energy of 4.5 MeV, there is a contribution from the three body interaction and other excited states in the neutron production from the main neutron group [4, 5]. Hence, the neutron spectrum produced from the $^{7}Li(p,n)$ reaction has contributions from sub-neutron groups in the main peak. The primary neutron peak has a higher neutron energy and flux which is used for the cross section measurements. The neutron spectrum for energies between 10-20 MeV are presented in *Figure 5.2* derived by interpolation technique using the spectrum reported by M. W. Mcnaughton et al. [21]. These neutron spectra were used by researchers of different groups [22-25] for the reaction cross section measurements. As shown in *Figure 5.2,* the neutron spectra have a quasi mono-energetic peak around E_p-1.881 MeV and a tail in a lower neutron energy region. The spectrum averaged neutron energy can be calculated using equation [26],

$$< E_{mean} > = \frac{\int_{E_{ps}}^{E_{max}} E_i \Phi_i dE}{\int_{E_{ps}}^{E_{max}} \Phi_i dE} \tag{5.1}$$

Where, E_{mean} is effective mean energy, E_{ps} is starting of peak neutron energy, E_{max} is maximum neutron energy, E_i is energy bin and Φ_i is neutron flux of energy bin E_i. The spectrum averaged neutron energies derived from the above formula for the different proton beam energies used in the experiments are given in *Table 5.1.* The reaction cross sections of ^{90}Zr , ^{93}Nb, ^{88}Sr and ^{85}Rb isotopes at different spectrum neutron energies are presented in the following sections.

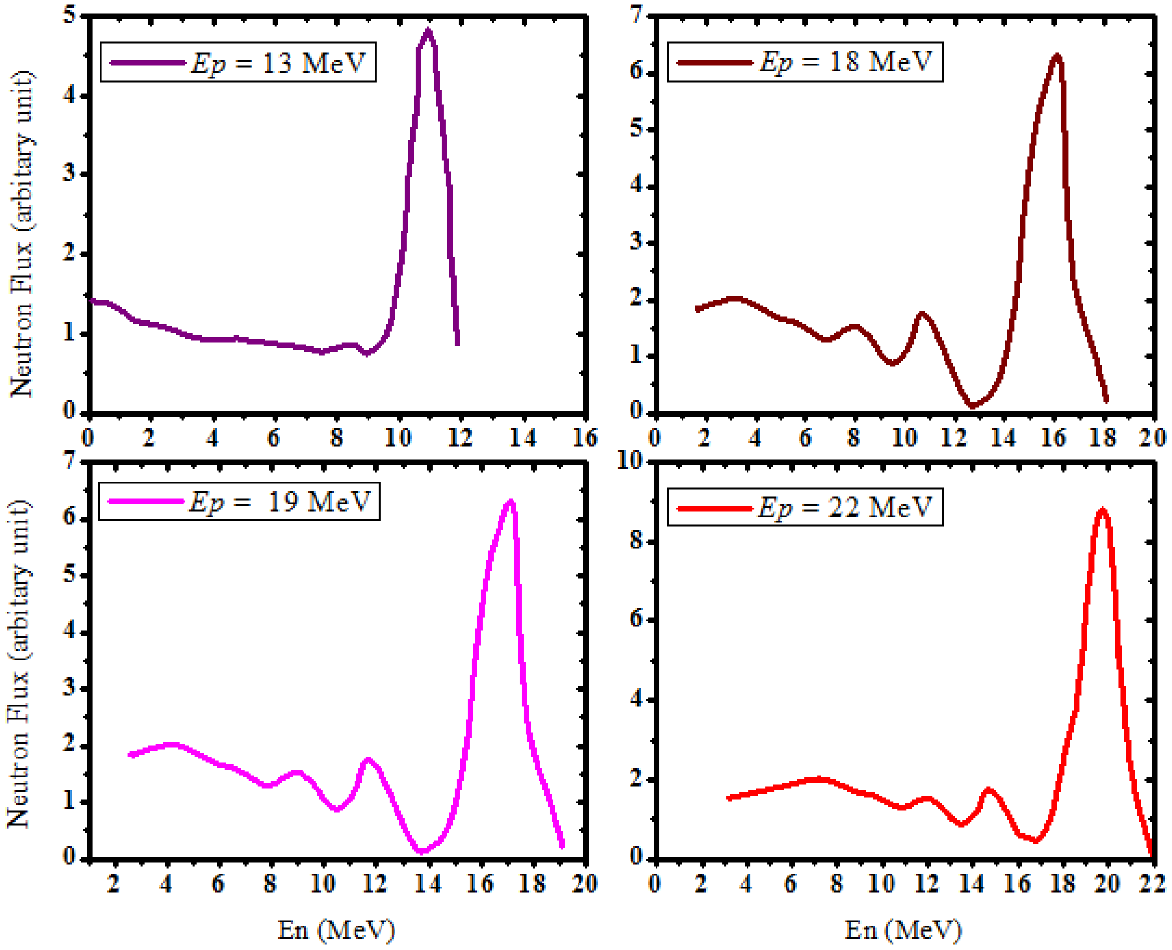

Figure 5.2 Neutron spectra from ^{7}Li(p,n)^{7}Be reaction at proton energies of 13, 18, 19 and 22 MeV generated from M.W. Mcnaughton et al. [21]

5.3 Cross section of ^{90}Zr(n,2n)^{89}Zr and ^{90}Zr(n,p)^{90m}Y reactions

Zirconium (Zr) and its alloys are extensively used as cladding material for fuel assemblies in fission reactors. In International Thermonuclear Experimental Reactor (ITER) like fusion reactors, these materials are used as structural materials. In designing of accelerator driven systems (ADS), Zr has been used as nuclear fuel pellets due to its properties such as low neutron capture cross section and corrosion resistance. It is also utilized as a primary target material for production of medical isotopes [27-30]. Because of the vast diversity of the Zr material, accurate knowledge of nuclear data is important to require for the design and operation of fission-fusion reactors, accelerators and also for medical applications. Since neutrons are generated in the operation of the reactors and accelerators, the reaction cross section data had a key role in damage studies, activation and nuclear transmutation studies [31-33]. In the present studies, the (n,2n) and (n,p) reactions cross section are determined in the fast neutron energy range by neutron activation technique followed by off line γ-ray spectroscopy. The ^{90}Zr(n,2n)^{89}Zr reaction cross section is determined at average neutron energies of 13.97 ± 0.68, 16.99 ± 0.53 and 20.02 ± 0.58 MeV and the cross sections of the ^{90}Zr(n,p)^{90m}Y reaction were measured at 10.95 ± 0.45, 13.97 ± 0.68, 16.99 ± 0.53 and 20.02 ± 0.58 MeV. The measured cross section data are compared to the previously published data available in EXFOR [7] data base and with ENDF/B-VIII.0, JEFF-3.3, JENDL-4.0 and ROSFOND-2010 [10-13] data files. Theoretically, the reaction cross sections are calculated by using TALYS-1.9 [8] and EMPIRE-3.2.2 [9] nuclear codes.

5.3.1 Data Analysis

In the present experiment, zirconium was used in natural form. Zirconium of purity (99.999 %) was used as a foil strip. It has isotopes with abundance ^{90}Zr (51.45%), ^{91}Zr (11.22%), ^{92}Zr (17.15%), ^{94}Zr (17.38%) and ^{96}Zr (2.80%). The dimension of zirconium foil was 10 × 10 × 0.3 mm used in all experiments. Aluminium (Al) and Indium (In) metal foils of a

Table 5.2 Sample and monitor details used for the present experiment

Sample	Isotope	Isotopic abundance (%)	Density (g/cm^3)	E$_n$ (MeV)	Weight (gm)	Number of target atoms (×10^{-4} atoms/b)
Al-foil	^{27}Al	100	2.7	10.95 ± 0.45	0.0125	2.789
				13.97 ± 0.68	0.0134	2.991
				16.99 ± 0.53	0.0125	2.789
				20.02 ± 0.58	0.0134	2.991
In-foil	^{115}In	95.71	7.31	10.95 ± 0.45	0.2391	11.99
				13.97 ± 0.68	0.1757	8.814
				16.99 ± 0.53	0.1791	8.986
				20.02 ± 0.58	0.2161	10.84
Zr foil	^{90}Zr	51.45	6.49	10.95 ± 0.45	0.185	6.290
				13.97 ± 0.68	0.287	9.744
				16.99 ± 0.53	0.192	6.515
				20.02 ± 0.58	0.185	6.290

purity ^{27}Al (100%) and ^{115}In (95.71%) with dimensions of $10 \times 10 \times 0.1$ mm^3 were used as monitors to measure the absolute neutron flux. The details of samples were given in *Table 5.2*. The area corrections in the flux values were minimized by preparing the target and monitor samples of the same dimensions. To avoid radioactive contamination during the experiment, the samples were wrapped in 0.025 mm thick aluminum foil. All samples were stacked and also wrapped additionally in aluminium foil of same thickness to avoid radioactive contamination to the surrounding. The target samples were positioned behind Ta-Li-Ta stack at a distance of 2.1 cm, at a 0^o angle in forward direction of the beam. The In-Zr-Al stacks were irradiated with the proton beam of energies 13, 16, 19 and 22 MeV, respectively.

Measurement of γ-ray activity

The samples were cooled for a sufficient time after the irradiation stop, to avoid the gamma dose from short-lived products. For the samples to exhibit sufficient activity, the irradiation was carried out for five to ten hours. The irradiated target samples with monitor were put on Perspex plates and placed on a detector for offline γ-ray spectroscopy. The induced activity in the samples was measured by a pre-calibrated 80 cm^3 high purity germanium (HPGe) detector having 1.82 keV energy resolution at 1332.50 keV γ-line of ^{60}Co. During the counting the dead time of the detector was kept < 5%. The γ-ray spectrum was recorded and analysed with a PC-based 4096 channel analyser having GENIE spectroscopic software. The nuclear spectroscopic data with uncertainties are given in *Table 5.3* [34-39]. The typical γ-ray spectrum recorded by the HPGe detector was presented in *Figure 5.3* and *Figure 5.4.*

Table 5.3 Nuclear spectroscopic data with uncertainties used in present experiment

Nuclear reaction	Threshold energy E_{th} (MeV)	Half-life of product (hour)	Eγ (keV)	Iγ (%)
^{27}Al(n,α)^{24}Na	3.249	14.997 ± 0.012	1368.63 ± 0.05	99.9936 ± 0.0005
^{115}In(n,n')^{115m}In	--	4.486 ± 0.004	336.24 ± 0.25	46.0 ± 0.2
^{90}Zr(n,2n)^{89}Zr	12.102	78.41 ± 0.12	909.15 ± 0.15	99.04 ± 0.03
^{90}Zr(n,p)^{90m}Y	1.512	3.19 ± 0.06	202.53 ± 0.03 479.51 ± 0.05	97.3 ± 0.4 90.74 ± 0.05

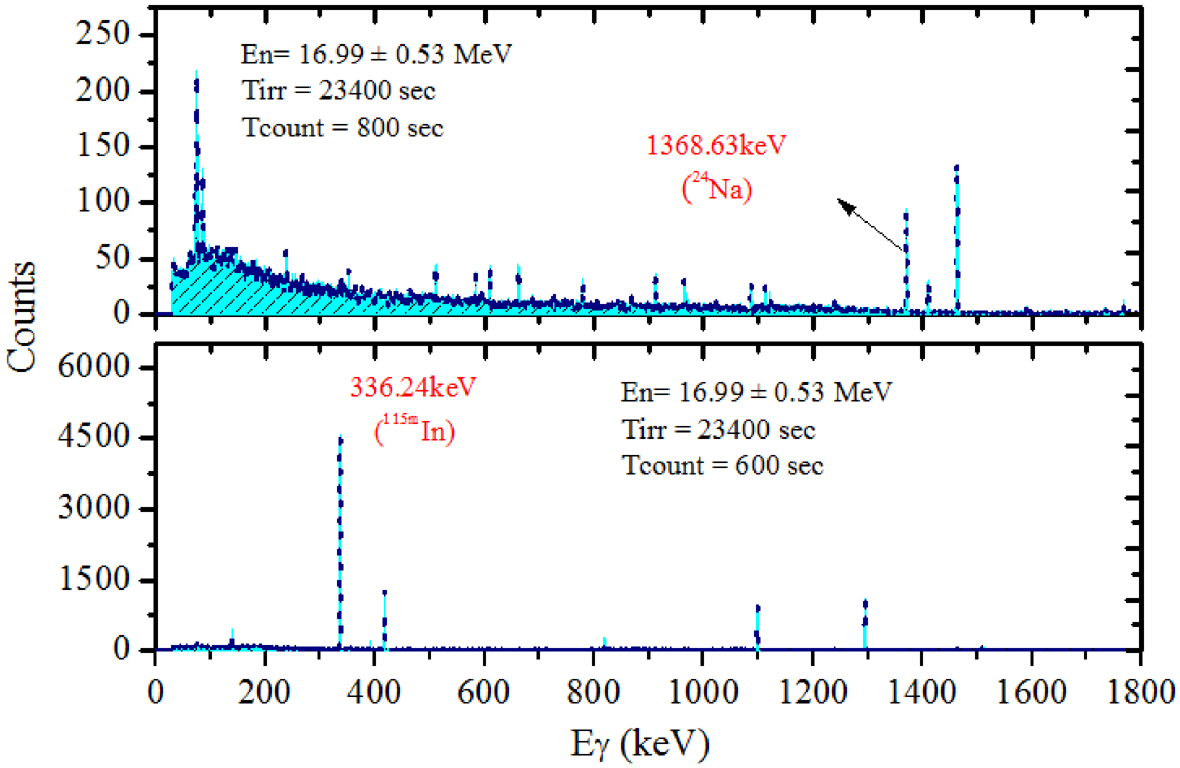

Figure 5.3 A typical γ-ray spectrum of $^{27}Al(n,\alpha)^{24}Na$ and $^{115}In(n,n')^{115m}In$ monitor reactions recorded by HPGe detector

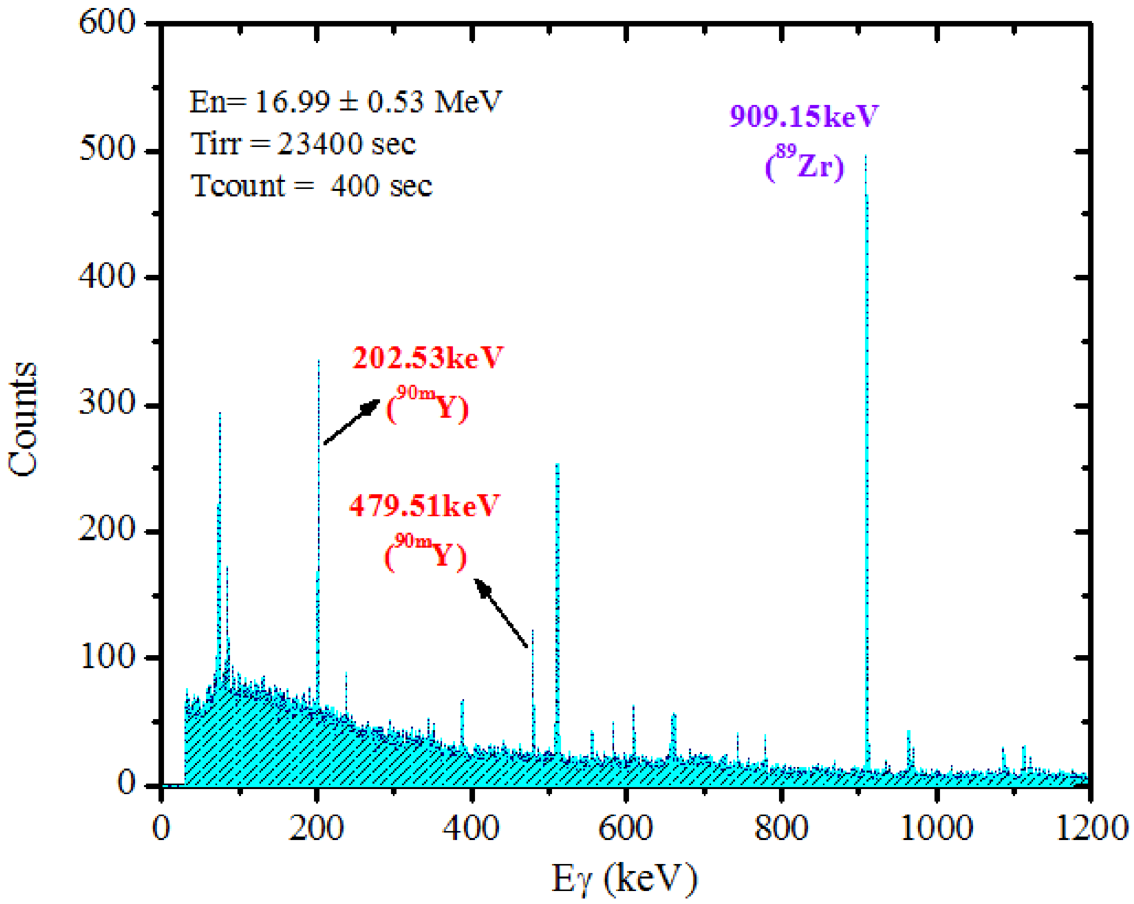

Figure 5.4 A typical γ-ray spectrum of $^{90}Zr(n,2n)^{89}Zr$ *and* $^{90}Zr(n,p)^{90m}Y$ *reactions recorded by HPGe detector*

The HPGe detector efficiency calibration for different γ-ray energies was determined using standard ^{152}Eu source [40] (A_0= 7767.73 ± 86.99 Bq. on 1-October-1999, $T_{1/2}$ = 13.517 ± 0.014 year). The following relation was used to calculate the detection efficiency.

$$\varepsilon = \frac{C_{obs} K_c}{A_0 I_\gamma e^{-\lambda T} \nabla t} \tag{5.2}$$

Where, C_{obs} is the number of counts measured in time (Δt = 5562 sec), I_γ is the absolute intensity for a particular γ-ray energy, A_0 is the activity of the ^{152}Eu-source at the time of manufacturing, T is the time interval between the source manufacturing to the experiment date. *Kc* is the coincidence summing correction factor. Since there was a minimum distance between the irradiated sample and the detector end cap, the correction for the coincidence summing effects of γ-ray energy lines was made for efficiency measurements. The Monte Carlo simulation code EFFTRAN [41] was used to calculate the correction factor (*Kc*). The code required the material and dimension details of crystal, cavity, housing, window and mounting holder of the HPGe detector and calibration source [42, 43]. The detector efficiency for the characteristic γ-ray energies of ^{152}Eu source with correction factor (K_c) was given in *Table 5.4.* The measured efficiency and the corrected efficiency were compared in *Figure 5.5.*

Table 5.4 HPGe detector efficiency with summing correction factors

Eγ (keV)	*Iγ*	Counts (C_{obs})	*Kc*	Efficiency	Efficiency with *Kc*
121.78	0.2853 ± 0.0016	490738 ± 736	1.186	0.0985	0.1168
244.69	0.0755 ± 0.0004	77343 ± 301	1.277	0.0585	0.0747
443.96	0.0282±0.00014	19807 ± 160	1.274	0.0403	0.0513
964.079	0.1451 ± 0.0007	52965 ± 243	1.129	0.0208	0.0265
1112.07	0.1367 ± 0.0008	45389 ± 226	1.068	0.0191	0.0204
1408.006	0.2087 ± 0.0009	57288 ± 246	1.095	0.0156	0.0164

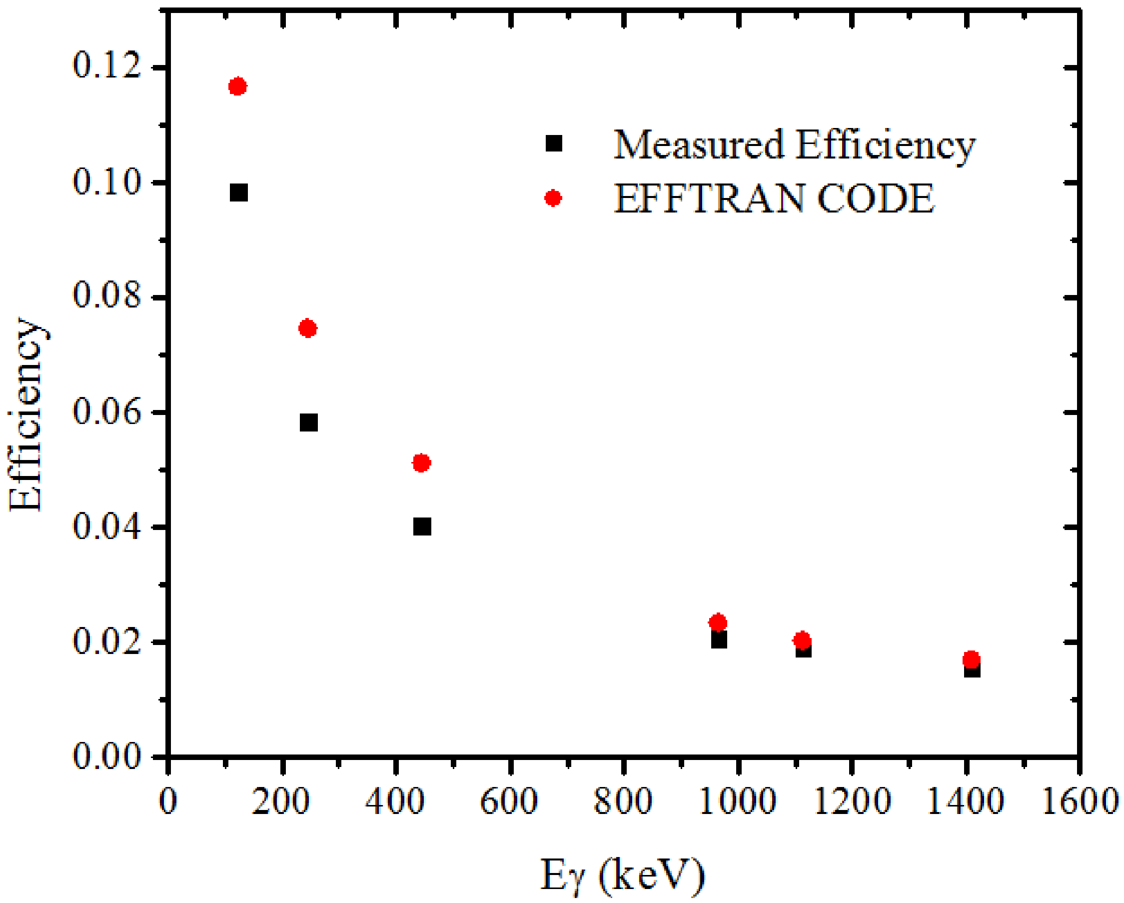

Figure 5.5 Comparison of the measured HPGe detector efficiency and EFFTRAN corrected efficiency

Covariance analysis and uncertainty propagation in detector efficiency

The detector efficiency was determined by four qualities, namely C_{obs}, A_0, I_γ, and $T_{1/2}$, as indicated by Eq. (5.2). Consequently, uncertainties in these variables would result in a propagation of detector efficiency estimation errors. The effectiveness can be increased by,

$$\left(\frac{\Delta\varepsilon_i}{\varepsilon_i}\right)^2 = \left(\frac{\Delta C_i}{C_i}\right)^2 + \left(\frac{\Delta I_{\gamma i}}{I_{\gamma i}}\right)^2 + \left(\frac{\Delta A_0}{A_0}\right)^2 + (t\Delta\lambda)^2 \quad (5.3)$$

Where, ΔC_i, $\Delta I_{\gamma i}$ *and* A_0 are the uncertainties in counts, γ-ray intensities and source activities respectively, and $\Delta\lambda = 0.693 \times \Delta T_{1/2}/T_{1/2}^2$ is the uncertainty in the decay constant. The partial uncertainties values are important to create the covariance matrix for the detector efficiencies which is determined by,

$$(V_\varepsilon)_{ij} = \sum_r e_{ir} S_{ijr} e_{jr} \quad (5.4)$$

Where, e_{ir} and e_{jr} are the n × n diagonal matrices and S_{ijr} are the n × n micro-correlation matrix. The partial uncertainties of four attributes were given in *Table 5.5*. The covariance matrix calculated using Eq. (5.3) and (5.4) were given in *Table 5.6.*

Table 5.5 Partial uncertainties of parameters used to obtain HPGe detector efficiency

Eγ (keV)	*Counts (C_{obs})*	*I_γ*	*Activity (A_0)*	*Half-life ($T_{1/2}$)*	Total uncertainty ($\times 10^{-3}$)
121.78	0.000816	0.000572	0.001155	4.83E-06	1.743638
244.69	0.000783	0.000329	0.000703	2.94E-06	1.221808
443.96	0.000688	0.002138	0.000488	2.04E-06	0.946682
964.079	0.000265	0.000107	0.00025	1.05E-06	0.425977
1112.07	0.000258	0.000117	0.000226	9.43E-07	0.396565
1408.006	0.000182	0.0000713	0.000187	7.83E-07	0.308867

Table 5.6 Covariance matrix ($V_{\epsilon_{ij}}$ × 100) for the detector efficiency

Eγ (keV)	**Covariance matrix**					
121.8	0.0030938					
244.7	0.0008305	0.0015126				
443.9	0.0005763	0.0003507	0.0009057			
964	0.0002955	0.0001798	0.0001248	0.000184		
1112	0.0002664	0.0001621	0.0001125	0.0000577	0.0001593	
1408	0.0001346	0.0001346	0.0009340	0.00004790	0.0000432	0.0000968

Since the γ-ray energy emitted from ^{89}Zr, ^{90m}Y, ^{24}Na, and ^{115m}In nuclides in this experiment varied, the linear interpolation approach was used to calculate the detector efficiency for the γ-ray energies. The fitting function used to determine the γ-ray energies' efficiency (Eγ) was provided by,

$$\ln \varepsilon_i = \sum_m P_m \ (\ln E_i)^{m-1} \tag{5.5}$$

Where, ε_i is the efficiency value considered for the cross section calculations, P_m is the fitting parameter of order m and E_i is the corresponding γ-ray energy. The above Eq. (5.5) can be written as Z = AP, with fitting parameters P_m and the corresponding covariance matrix V_p, is given as,

$$P_m = V_p\ (A^T V_Z^{-1} A)\ ; V_p = \ (A^T V_Z^{-1} Z) \tag{5.6}$$

where, V_z matrix can be obtained as,

$$V_Z = \frac{\left(V_{\varepsilon_{ij}}\right)}{< \varepsilon_i >< \varepsilon_j >}$$

The goodness of the fit can be obtained as,

$$\chi_m^2 = (Z - AP)' V_Z^{-1} (Z - AP) \tag{5.7}$$

By using above definitions, the fitting parameters for the detector efficiencies of sample and monitor reaction residues γ-rays were found to be

$$P_m = (-0.38370; -0.8694;\ 0.1693;\ 0.3208; -0.10)\ ;\quad \chi_m^2 = 0.72$$

The detector efficiencies determined from the above fitting parameters for ^{89}Zr, ^{90m}Y, ^{115m}In and ^{24}Na nuclides with corresponding correlation parameters [22-24] are given in *Table 5.7* and *Figure 5.6* displays the fitted efficiency curve and the measured efficiency based on the aforementioned fitting parameters.

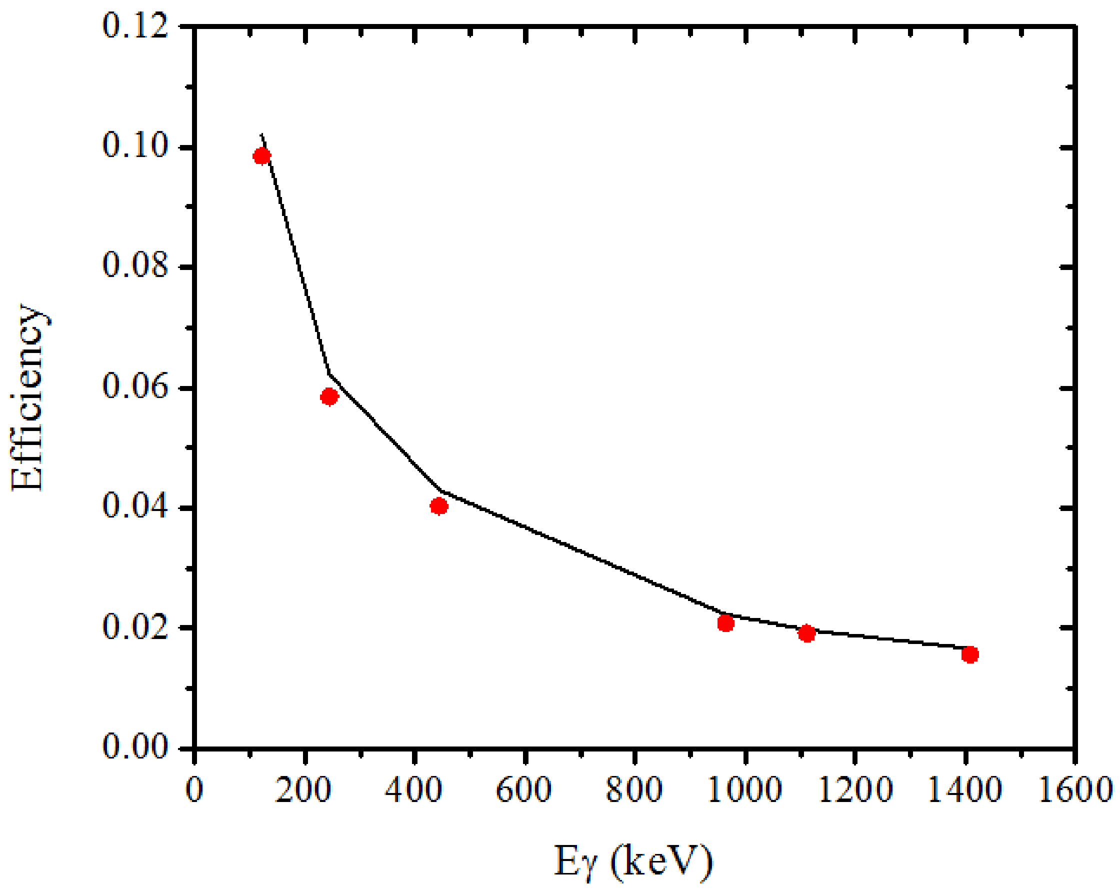

Figure 5.6 Efficiency fitted curve and the measured efficiency

Table 5.7 Interpolated detection efficiencies with uncertainties and correlation matrices for sample and monitor reactions

Reaction	Eγ (keV)	Efficiency	Error	Correlations					
^{90}Zr(n,p)^{90m}Y	202.53	0.069118	0.001639	0.2686	1.				
^{115}In(n,n')^{115m}In	336.24	0.051709	0.000963	0.0569	0.360	1.			
^{90}Zr(n,p)^{90m}Y	479.51	0.040575	0.000891	-0.0093	-0.064	0.876	1.		
^{90}Zr(n,2n)^{89}Zr	909.15	0.023447	0.000397	0.0181	0.279	0.436	0.547	1.	
^{27}Al(n,α)^{24}Na	1368.6	0.016727	0.000295	0.0135	0.281	0.419	0.306	0.359	1.

Estimation of ^{90}Zr(n,2n)^{89}Zr and ^{90}Zr(n,p)^{90m}Y reactions cross section

Using offline γ-ray spectrometry and the neutron activation technique, the reactions cross section was obtained. The activation formula was utilized to compute the reaction cross section based on the photo peak's γ-ray counts in the recorded spectra,

$$< \sigma_R >= \frac{C_\gamma \lambda\left(\frac{CL}{LT}\right)}{N\Phi I_\gamma \varepsilon\left(1-e^{-\lambda t_i}\right)\left(1-e^{-\lambda t_c}\right)e^{-\lambda t_r}} \tag{5.8}$$

where, C_γ: number of counts of photo peak, λ: decay constant (s^{-1}), *CL* and *LT*: clock time and live time for counting and *CL/LT* term is for dead time correction, *N*: number of atoms in target material, Φ: neutron flux, I_γ: absolute γ-ray intensity per decay of the residual nucleus (taken from Ref. [24]), ε: photo peak efficiency of the γ-rays, t_i: irradiation time and tc: cooling time.

Table 5.3 summarizes the nuclear spectroscopic data that were used to calculate the ^{90}Zr(n,2n)^{89}Zr and ^{90}Zr(n,p)^{90m}Y reactions [38, 39]. Neutron energies of 13.97 ± 0.68, 16.99 ± 0.53, and 20.02 ± 0.58 MeV were used to measure the reaction cross sections since the ^{90}Zr(n,2n)^{89}Zr reaction threshold energy (Eth) is 12.102 MeV. The ^{89}Zr product nuclide decays with an energy of 909.15 keV γ-rays and has a half-life of 78.41 ± 0.12 h. Based on the observed activity of γ-ray energy of ^{89}Zr from the recorded γ-ray spectra with adequate cooling time, the cross section of the ^{90}Zr(n,2n)^{89}Zr reaction was calculated. Comparably, the ^{90}Zr(n,p)^{90m}Y reaction has a threshold energy (E_{th}) of 1.512 MeV; hence, the reaction cross sections were measured at neutron energies of 10.95 ± 0.45, 13.97 ± 0.68, 16.99 ± 0.53 MeV, and 20.02 ± 0.58 MeV. The ^{90m}Y product nuclide, whose half-life is 3.19 ± 0.06 h, was responsible for the observed activity of γ-ray energies of 202.53 keV and 479.51 keV, which was used to measure the cross section.

Tailing correction

The lower energy neutrons in this experiment contributed to the measured reaction cross section; hence, by subtracting the contribution from the lower energy neutrons, the accurate reaction cross section for the major peak neutrons was found. *Figure 5.7* showed the neutron energy spectrum of a 22 MeV proton beam. The tailing correction method was used to make the necessary changes to the measured cross section values. According to the literature, this approach eliminated the contribution from the tail portion [25, 26]. This was accomplished by estimating the cross section from the low energy neutrons using the TALYS-1.9 code [8]. The associated neutron spectrum's neutron flux distribution was folded with the cross section values. The following relation was used to compute the cross section due to the tail component.

$$< \sigma_{tail} > = \frac{\int_{E_{th}}^{E_{ps}} \sigma(\mathrm{E})\Phi(\mathrm{E})dE}{\int_{E_{th}}^{E_{ps}} \Phi(\mathrm{E})dE} \tag{5.9}$$

Where, E_{th}: threshold energy of the corresponding reaction and E_{ps}: minimum energy of the main peak for the different proton energies.

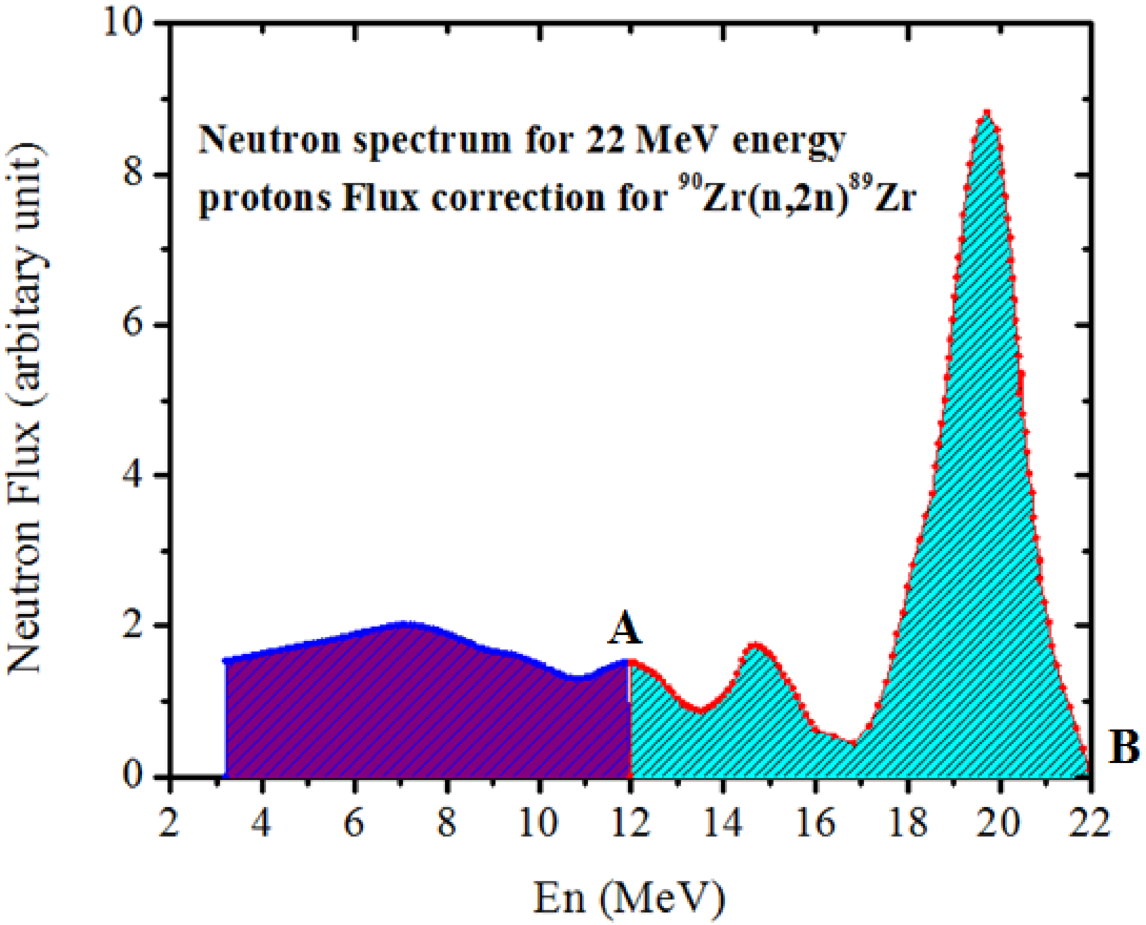

Figure 5.7 Tailing correction for reactions having threshold energy

Since both reactions in this instance have threshold energies, the adjusted neutron flux has been utilized to determine the true cross section. The threshold energy (E_{th}) of ^{90}Zr(n,2n)^{89}Zr reaction is 12.102 MeV, in order to calculate the reaction cross section, one must first calculate the neutron flux, which is represented by the area under the curve from A (E_{th}) to B (E_{max}), as shown in *Figure 5.7*. By predicting the matching reaction cross section using the TALYS-1.9 algorithm from the threshold energy, or E_{th} (point A), to the minimum energy at which the major peak commenced, or E_{ps} (point B), the lower energy tail part contribution from the measured findings was recovered. The spectrum averaged reaction cross section determined from Eq. (5.9) was subtracted from the calculated cross section values to obtain the final cross section values for the main peak neutron energy. The corrected cross section values for the ^{90}Zr(n,p)^{90m}Y reaction was determined in similar manner at neutron energies 10.95 ± 0.45, 13.97 ± 0.68, 16.99 ± 0.53 and 20.02 ± 0.58 MeV. *Table 5.8* presents a comparison between the measured cross section for both reactions and the earlier published results.

Table 5.8 Comparison of reaction cross sections with published data

<table>
<tr><th colspan="5">^{90}Zr(n,2n)^{89}Zr reaction cross section (mbarn)</th></tr>
<tr><th>En (MeV)</th><th>Measured</th><th>Tailing correction</th><th>Final</th><th>Published Data[3]</th></tr>
<tr><td>13.97 ± 0.68</td><td>515.24</td><td>-</td><td>515.2 ± 37.4</td><td>539.7 ± 11.9 Jiuzi et al. [66]</td></tr>
<tr><td>16.99 ± 0.53</td><td>1118.88</td><td>107.08</td><td>1011.8 ± 72.94</td><td>1086 ± 36 Pavlik et al. [67]</td></tr>
<tr><td>20.02 ± 0.58</td><td>1633.88</td><td>542.78</td><td>1091.1 ± 78.66</td><td>1200 ± 80 Semkova et al. [65]</td></tr>
<tr><th colspan="5">^{90}Zr(n,p)^{90m}Y reaction cross section (mbarn)</th></tr>
<tr><td>10.95 ± 0.45</td><td>6.72</td><td>0.83</td><td>5.89 ± 0.41</td><td>5.41 ± 0.07 Raics et al. [75]</td></tr>
<tr><td>13.97 ± 0.68</td><td>9.71</td><td>0.86</td><td>8.85 ± 0.64</td><td>11.8 ± 0.6 Filatenkov [64]</td></tr>
<tr><td>16.99 ± 0.53</td><td>13.74</td><td>1.51</td><td>12.23 ± 0.88</td><td>12.1 ± 0.2 Marcinkowski et al. [76]</td></tr>
<tr><td>20.02 ± 0.58</td><td>10.69</td><td>3.24</td><td>7.45 ± 0.54</td><td>8.4 ± 0.8 Semkova et al. [65]</td></tr>
</table>

Reference monitor cross section

The monitor reaction for cross section measurements was selected in compliance to the threshold energy of the reactions. In present calculations, the 336.24 keV γ-ray energy from

---

[3] Published data are near to the values of present work

^{115In}(n,n'γ)^{115m}In reaction was selected for ^{90}Zr(n,p)^{90m}Y reaction and 1368.63 keV γ-ray energy from ^{27}Al(n,α)^{24}Na was selected for ^{90}Zr(n,2n)^{89}Zr reaction. The spectrum averaged cross section for monitor reactions was calculated to estimate the absolute neutron flux using equation,

$$\sigma_{av} = \frac{\int_{E_{th}}^{E_{max}} \sigma_i \Phi_i dE}{\int_{E_{th}}^{E_{max}} \Phi_i dE} \tag{5.10}$$

Where, σ_{av} is a spectrum averaged cross section, σ_i is a cross section at energy E_i for monitor reaction taken from EXFOR data [8], E_{th} is the threshold energy of monitor reaction calculated from Q-calculator [34, 35], E_{max} is the maximum neutron energy and Φ_i is neutron flux.

Table 5.9 Spectrum averaged cross section and neutron flux from different monitor reaction

En (MeV)	**10.95 ± 0.45**	**13.97 ± 0.68**	**16.99 ± 0.53**	**20.02 ± 0.58**
Measured neutron flux based on the ^{27}Al(n,α)^{24}Na reaction monitor (n cm^{-2} s^{-1})	1.3237 x 10^6	1.1706 x 10^6	2.4549 x 10^6	3.3569 x 10^6
Measured neutron flux based on the ^{115}In(n,n')^{115m}In reaction monitor (n cm^{-2} s^{-1})	1.3343 x 10^6	1.1980 x 10^6	2.4621 x 10^6	3.3939 x 10^6

The neutron flux (Φ) incident on target samples was calculated by using the following activation equation.

$$\Phi = \frac{C_\gamma \lambda \left(\frac{CL}{LT}\right)}{N \sigma_{av} I_\gamma \varepsilon \left(1-e^{-\lambda t_i}\right)\left(1-e^{-\lambda t_c}\right) e^{-\lambda CL}} \tag{5.11}$$

Where, C_γ is the number of counts of photo peak, λ is the decay constant (sec^{-1}), N is the number of atoms in target material, σ_{av} is the spectrum averaged cross section (derived from Eq. (5.8)), I_γ is the absolute γ-ray intensity per decay of the residual nucleus (taken from ref. [24]), ε is the photo peak efficiency of the γ-rays, t_i is irradiation time, t_c is cooling time, *CL* and *LT* are clock time and live time for counting. The *CL/LT* term is used for dead time correction. The measured neutron flux from the ^{27}Al(n,α)^{24}Na and ^{115}In(n,n')^{115m}In monitor reactions for all four neutron energies are given in *Table 5.9*.

Covariance analysis and uncertainty propagation in the reaction cross section

According to refs. [6, 44], the covariance analysis was performed using the ratio method to determine the reaction cross section. The Eqs. (5.8) and (5.11) can be rewrite as,

$$\sigma_R = \sigma_m \frac{C_s N_m \Phi_m I_{\gamma m} \varepsilon_m f_{\lambda m}}{C_m N_s \Phi_s I_{\gamma s} \varepsilon_s f_{\lambda s}} \tag{5.12}$$

Where, the terms have the meanings similar to Eq. (5.8). The subscript ‘s’ denotes for sample reaction parameters and ‘m’ denotes for monitor reactions parameters and the time factor ‘*f*’ and $'\eta_{m,s}'$ are defined as,

$$f = \left(1 - e^{-\lambda t_i}\right)\left(1 - e^{-\lambda t_c}\right)\left(e^{-\lambda t_r}\right)/\lambda \tag{5.13}$$

Using $N = MN_A a/A$ for atoms in target material, where M is the sample weight, N_A is the Avogadro number, a is the abundance and A is the atomic mass, the Eq. (5.12) was,

$$\sigma_R = \sigma_m \frac{C_s M_m a_m A_s I_{\gamma m} \varepsilon_m f_{\lambda m}}{C_m M_s a_s A_m I_{\gamma s} \varepsilon_s f_{\lambda s}} \tag{5.14}$$

The partial uncertainties from each attribute in above equation can be communicated directly to the sample cross section using the quadratic sum formula. The decay constant because of its relation to the cross section by an exponential function, the uncertainty in time factor (*f*) can be denoted as,

$$\left(\frac{\nabla f}{f}\right)^2 = \left(\frac{\lambda t_i e^{-\lambda t_i}}{1-e^{-\lambda t_i}} - \lambda t_c + \frac{\lambda(LT) e^{-\lambda(LT)}}{1-e^{-\lambda(LT)}} - 1\right)\left(\frac{\nabla \lambda}{\lambda}\right)^2 \tag{5.15}$$

The detector efficiency ratio for sample and monitor reactions is $\eta_{m,s} = \frac{\varepsilon_m}{\varepsilon_s}$ and the uncertainty is introduced by,

$$\frac{\nabla \eta_{m,s}}{\eta_{m,s}} = Var(\varepsilon_m) + Var(\varepsilon_s) - 2Cov(\varepsilon_m, \varepsilon_s) \tag{5.16}$$

By using the method described above, the covariance matrix ($V_{(CS)ij}$) was calculated for the reaction cross section values. The partial uncertainties propagated from all parameters in Eq. (5.14) with the corresponding correction factors for the $^{90}Zr(n,2n)^{89}Zr$ reaction relative to $^{27}Al(n,\alpha)^{24}Na$ monitor reaction were given in *Table 5.10* and the covariance and the correlation matrices were given in *Table 5.11*. Similarly, the partial uncertainties with corresponding correction factors for the ^{90}Zr(n,p)^{90m}Y reaction with ^{115}In(n,n')^{115m}In monitor reaction were given in *Table 5.12* and the covariance and the correlation matrices were given in *Table 5.13.*

Table 5.10 Partial uncertainties of the ^{90}Zr(n,2n)^{89}Zr reaction cross section measurements with respect to the ^{27}Al(n,α)^{24}Na monitor reaction

Parameters	**Partial Uncertainty (%)**			**Correlation**
	En = 13.97 ± 0.68	En = 16.99 ± 0.53	En = 20.02 ± 0.58	
C_S	0.005073	0.002098	0.011467	0
C_m	0.0515	0.0669	0.07060	0
I_s	0.000303	0.000303	0.000303	1
f_s	0.114215	0.113844	0.114509	1
f_m	0.000639	0.000369	0.000336	1
W_s	0.011205	0.012162	0.019323	0
W_m	0.014230	0.019950	0.024890	0
σ_m	0.088126	0.071952	0.086428	0
a_s	0.000583	0.000583	0.000583	1
A_s	2.19×10^{-5}	2.19×10^{-5}	2.19×10^{-5}	1
A_m	4.45×10^{-9}	4.45×10^{-9}	4.45×10^{-9}	1
I_m	1.5×10^{-5}	1.5×10^{-5}	1.5×10^{-5}	1
$\eta_{m,s}$	0.000285	0.000285	0.000285	1

Table 5.11 The measured cross section data with uncertainties along with covariance and correlations matrices for ^{90}*Zr(n,2n)*^{89}*Zr reaction*

En (MeV)	**Cross section (mb)**	**Covariance**			**Correlations**		
13.97 ± 0.68	515.173 ± 79.507	0.0238			1.		
16.99 ± 0.53	1011.788 ± 153.992	0.0130	0.0232		0.553	1.	
20.02 ± 0.58	1091.078 ± 178.243	0.0131	0.0130	0.0267	0.518	1.0	1.

Table 5.12 Partial uncertainties of the ^{90}*Zr(n,p)*^{90m}*Y reaction cross section measurements with respect to the*^{115}*In(n,n'γ)*^{115m}*In monitor reaction*

Parameters	**Partial Uncertainty (%)**				**Correlation**
	En = 10.95 ± 0.45	En = 13.97 ± 0.68	En = 16.99 ± 0.53	En = 20.02 ± 0.58	
C_S	0.099	0.163	0.1509	0.204	0
C_m	0.012	0.0094	0.0071	0.0094	0
I_s	0.000551	0.000551	0.000551	0.000551	1
f_s	0.11422	0.14387	0.11314	0.11128	1
f_m	0.00097	0.00074	0.00021	0.00027	1
W_s	0.013	0.014	0.012	0.012	0
W_m	0.011	0.016	0.022	0.013	0
σ_m	0.035611	0.091730	0.16026	0.10467	0
a_s	0.000583	0.000583	0.000583	0.000583	1
a_m	0.000522	0.000522	0.000522	0.000522	1
A_s	2.19×10^{-5}	2.19×10^{-5}	2.19×10^{-5}	2.19×10^{-5}	1
A_m	4.35×10^{-8}	4.35×10^{-8}	4.35×10^{-8}	4.35×10^{-8}	1
I_m	0.002179	0.002179	0.002179	0.002179	1
$\eta_{m,s}$	0.036589	0.036589	0.036589	0.036589	1

Table 5.13 The measured cross section data with uncertainties along with covariance and correlations matrices for $^{90}Zr(n,p)^{90m}Y$ reaction

En (MeV)	Cross section (mb)	Covariance				Correlations			
10.95 ± 0.45	5.897 ± 1.014	0.0296				1.			
13.97 ± 0.68	8.854 ± 2.140	0.0162	0.0584			0.389	1.		
16.99 ± 0.53	12.232 ± 3.069	0.0127	0.0162	0.0630		0.293	0.267	1.	
20.02 ± 0.58	7.452 ± 1.922	0.0124	0.0159	0.0125	0.0665	0.280	0.255	0.193	1.

5.3.2 Theoretical calculations

The $^{90}Zr(n,2n)^{89}Zr$ and $^{90}Zr(n,p)^{90m}Y$ reactions were calculated theoretically from reaction threshold energy to 22 MeV using the TALYS 1.9 [13] and EMPIRE-3.2.2 [14] algorithms. The interaction of neutrons, protons, photons, deuterons, tritons, ^{3}He-, and α- particles with target nuclides of mass 5 and heavier in the energy range of 1 keV to 200 MeV [45] produced the nuclear data for all the reaction channels that were opened. A variety of nuclear models and build-up parameter options, including those assembled in the Reference Input Parameter Library RIPL-3 database, were used to create the reactions cross section [46]. In the current investigation, the local optical model potential (OMP) suggested by Koning et al. [47] was applied to the outgoing protons and neutrons. The Hauser-Feshback model is used by the TALYS code to account for compound nucleus contributions [48]. For the pre-equilibrium contribution, a two-component exciton model put forth by Koning and Duijvestijn [49] was employed. Furthermore, TALYS includes six distinct level density models, denoted as ldmodel-1 through ldmodel-6, to forecast reactions cross section [50–55].

The $^{90}Zr(n,2n)^{89}Zr$ and $^{90}Zr(n,p)^{90m}Y$ reactions cross sections from threshold to 22 MeV were also calculated using the EMPIRE-3.2.2 code. Based on several reaction mechanisms, this code offers accurate and comprehensive information about reaction cross sections [9, 56, 57]. The compound nucleus reaction cross sections were computed using the Hauser-Feshbach statistical model. The EMPIRE code offers many nuclear level density models (LEVDEN 0-3) with varying parameterizations for calculating the reaction cross section [9]. The ECIS06 code was used to create the optical model procedures that yielded the transmission coefficients [58, 59]. Spherical optical model calculations were carried out for the direct reactions. For outgoing protons and neutrons, the optical model values recommended by Koning et al. [47] and Morillon et al. [60] were used in these simulations. The Hofmann, Richert, Tepel, and Weiden muller (HRTW) model was applied up to an incident neutron energy of 3 MeV in order to account for the width fluctuation corrections [61]. The Modified Lorentzian (MLO1) γ-ray strength functions provided by Plujko [62] were utilized to characterize the gamma emission, with values sourced from the RIPL-3 database [37]. The classical exciton model [63] and the PCROSS code [9], with the default mean free path parameter (PCROSS-1.5), were used to represent the pre-equilibrium emission mechanism. The required input parameters for TALYS-1.9 and EMPIRE-3.2.2 input files, which are utilized to forecast the cross sections of the current investigation, are listed in *Table 5.14*.

Table 5.14 Basic keywords and the corresponding values used in the input file of the TALYS-1.9 and EMPIRE-3.2.2 code in order to reproduce the cross sections of present work

TALYS-1.9	EMPIRE-3.2.2
ldmodel 3	LEVDEN 3
widthmode 1	HRTW 3
widthfluc 11.968	GSTRFN 1
gammax 2	OMPOT 2411 1(n)
strength 1	OMPOT 5411 2(p)
localomp y	DIRECT 0
preeqmode 2	PCROSS 1.5

5.3.3 Results and Discussion

The cross section of the ^{90}Zr(n,2n)^{89}Zr and ^{90}Zr(n,p)^{90m}Y reactions were measured in this experiment using neutrons with energies between 10 and 20 MeV. The ^{7}Li(p,n)^{7}Be reaction produced the quasi-monoenergetic neutrons. The HPGe detector's efficiency was calibrated using a standard ^{152}Eu source that had characteristic γ-ray energies. *Table 5.9* lists the monitor reactions that were used to calculate the neutron flux: ^{115}In(n,n')^{115m}In and ^{27}Al(n,α)^{24}Na. When measuring the cross sections at various neutron energies, the correction factors in the neutron flux were taken into account. As seen in *Table 5.8*, the literature data [10-13, 64-68] at neutron energies comparable to those employed in the current work were included for comparison. Covariance analysis was used to calculate the uncertainties in the current measurements, which were found to be between 15 - 26%. The experimental results are compared in *Figs. 5.8* to *5.11* with measured data from EXFOR [7], predicted data from TALYS-1.9 [8] and EMPIRE-3.2.2 [9] algorithms with optimized parameters, and evaluated data [10–13]. The ^{90}Zr(n,2n)^{89}Zr reaction cross section at neutron energies of 13.97 ± 0.68 and 16.99 ± 0.53 MeV is shown in Table 5.8, and it is in good agreement with the cross section estimates published by A. Pavlik et al. (1982) [67] and Qiu Jiuzi et al. (1996) [66]. However, at 20.02 ± 0.58 MeV, present results show a slightly lower cross section compared to the findings from Semkova et al. [65] at 20.1 ± 0.1 MeV. Additionally, *Fig. 5.8 and 5.9* demonstrate the excellent agreement between the present experimental ^{90}Zr(n,2n)^{89}Zr reaction cross section and the earlier reported data from EXFOR [7], as well as evaluated data from ENDF/B-VIII.0 [10], JENDL-4.0 [11], JEFF-3.3 [12], and ROSFOND-2010 [13] libraries.

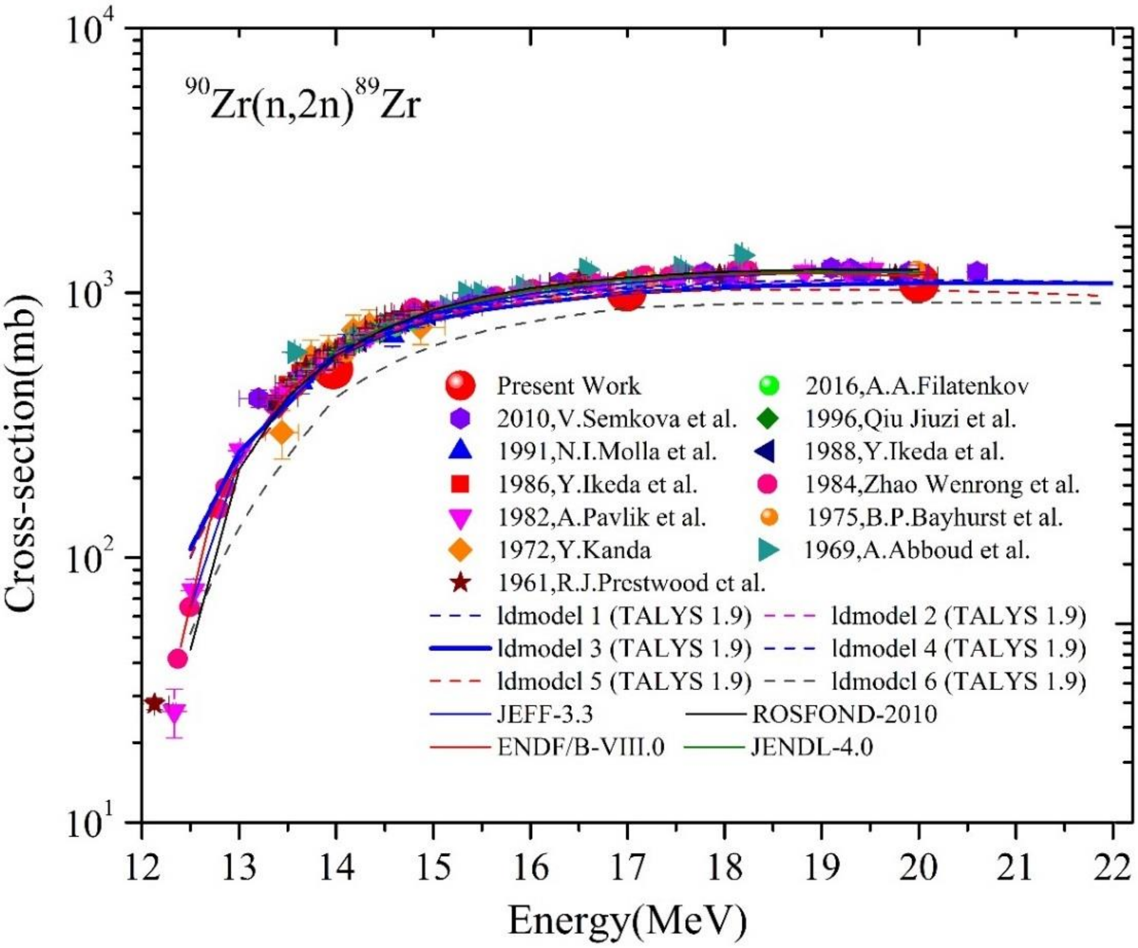

Figure 5.8 Comparison of experimental results of present work along with previously reported data in EXFOR [7], evaluated data [10-13] and theoretically calculated data by TALYS-1.9 code [8] for ^{90}Zr(n,2n)^{89}Zr reaction

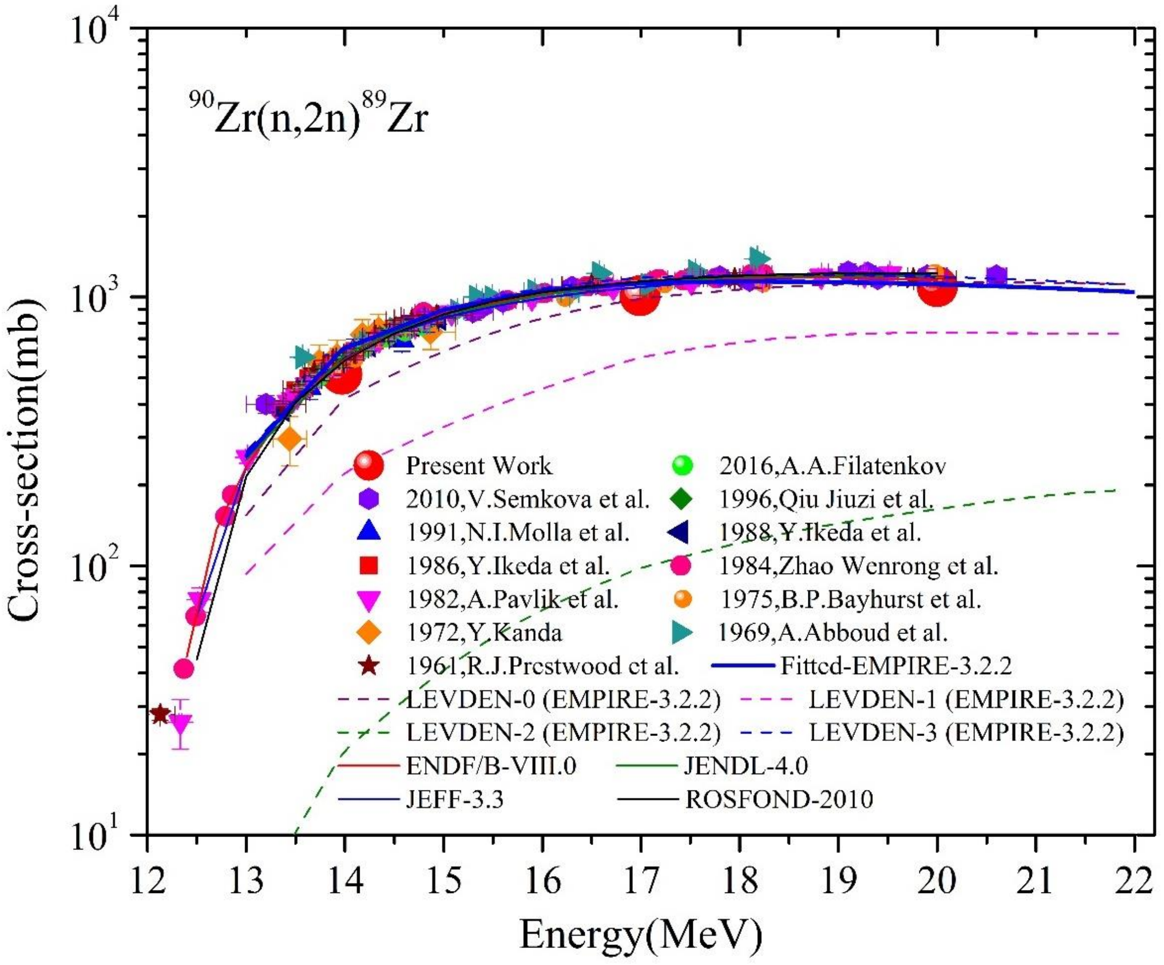

Figure 5.9 Comparison of experimental results of present work along with previously reported data in EXFOR [7], evaluated data [10-13] and theoretically calculated data by EMPIRE-3.2.2 code [9] for $^{90}Zr(n,2n)^{89}Zr$ reaction

Similarly, *Table 5.8* reveals a consistent agreement between the $^{90}Zr(n,p)^{90m}Y$ reaction cross sections obtained in this study and those previously measured by Raics et al. [75], Marcinkowski et al. [76] and Semkova et al. [65] at different neutron energies. Specifically, the cross section values at measured neutron energies in present study align well with the previous data. However, the $^{90}Zr(n,p)^{90m}Y$ reaction cross sections at the neutron energy of 13.97 ± 0.68 MeV is marginally lower than the data published by Filatenkov et al. [64] at 13.96 MeV. Furthermore, *Figures 5.8 to 5.11* demonstrate that the data fill in the blanks and adhere to the experimental data's trend line [64–80]. This consistency is also observed when comparing the measured data with the earlier published data from EXFOR [7] for

^{90}Zr(n,2n)^{89}Zr and ^{90}Zr(n,p)^{90m}Y reactions across a range of energies from threshold to 22 MeV. Theoretical values based on TALYS-1.9 [8] and EMPIRE-3.2.2 [9] codes also exhibit a similar trend. However, EMPIRE-3.2.2 with the Morillon et al. [60] and RIPL-3 microscopic HFB nuclear level density model (Fitted-EMPIRE) likewise matches the cross sections of the current investigation, while TALYS-1.9 with the generalized superfluid model matches the present results for both reactions.

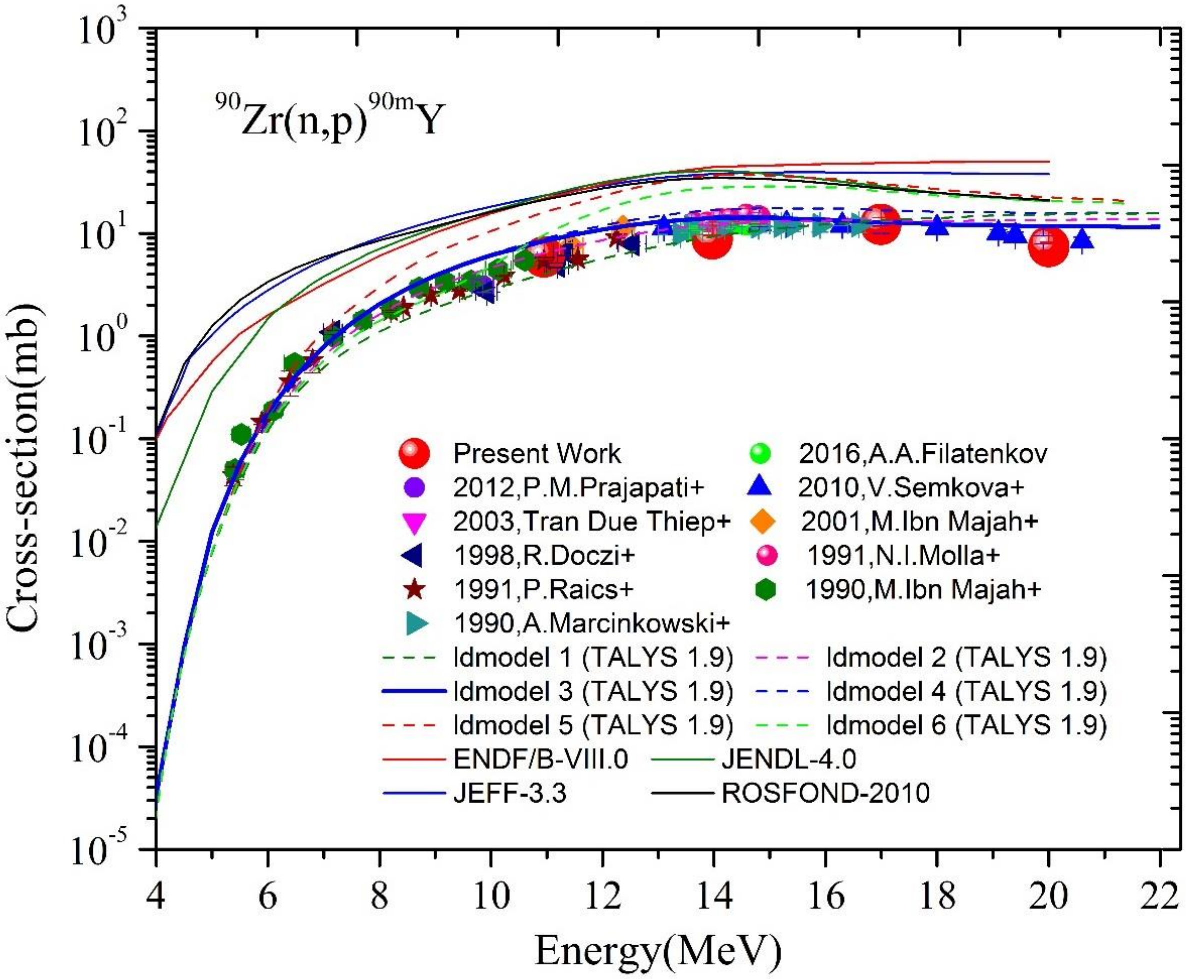

Figure 5.10 Comparison of experimental results of present work along with previously reported data in EXFOR [7], evaluated data [10-13] and theoretically calculated data by TALYS-1.9 code [8] for the ^{90}Zr(n,p)^{90m}Y reaction

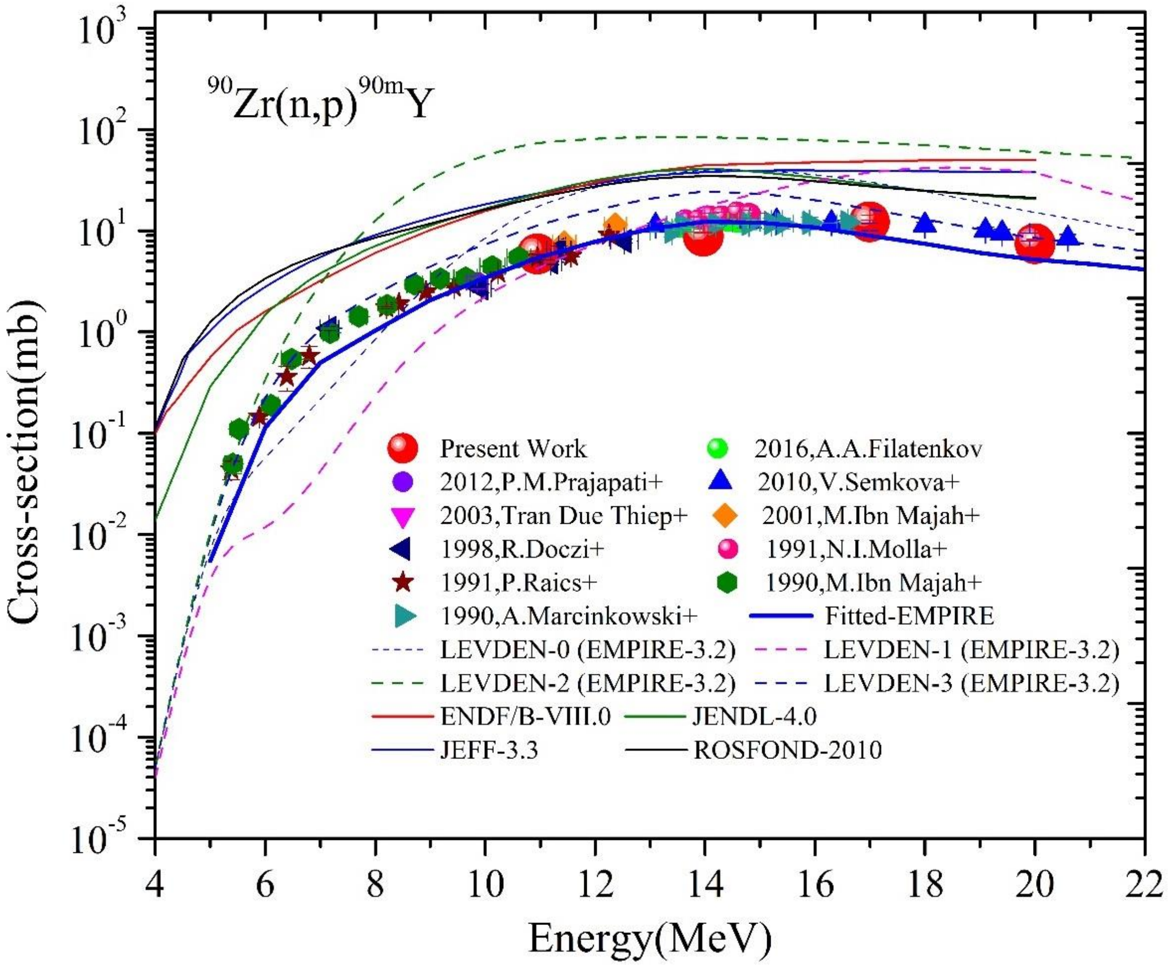

Figure 5.11 Comparison of experimental results of present work along with previously reported data in EXFOR [7], evaluated data [10-13] and theoretically calculated data by EMPIRE-3.2.2 code [9] for the $^{90}Zr(n,p)^{90m}Y$ reaction

5.4 Cross section of ^{93}Nb(n,2n)^{94m}Nb and ^{88}Sr(n,2n)^{87m}Sr reactions

Niobium (Nb) and Strontium (Sr) are the structural materials for fusion and fission reactors as well due to their super conductive properties Nb and Sr are prominent materials used as super-conducting magnets in the reactors. The ^{93}Nb(n,2n)^{92m}Nb reaction cross sections are also used as flux monitor and important in neutron dosimetry applications in 10 to 20 MeV energy range [81-87]. The cross section of ^{88}Sr(n,2n)^{87m}Sr reaction was previously reported by different authors around 14 MeV energy but very few data with discrepancies are available in neutron energy range between 15 to 20 MeV. [88-97] Therefore, it is necessary to obtain accurate cross sections data in this energy region. In this study, the cross sections of ^{93}Nb(n,2n)^{92}Nb^{m} reaction was determined at 13.97 ± 0.68 MeV and 20.02 ± 0.58 MeV and the ^{88}Sr(n,2n)^{87}Sr^{m} reaction cross section was determined at 13.97±0.68 MeV and 16.99 ± 0.53 MeV energies. These measurements were conducted using the activation and offline γ-ray spectrometry technique. To evaluate study results, the experimentally measured results were compared with the existing literature data in EXFOR database [7] and evaluated nuclear data from JEFF-3.3 [12], JENDL/AD-2017 [14] and TENDL-2019 [15]. Furthermore, the theoretical cross sections were predicated using TALYS-1.9 nuclear code [8].

5.4.1 Data Analysis

The ^{nat}Nb-foil of dimension $10 \times 10 \times 0.8$ mm^3 and natural Sr-foil of dimension $10 \times 10 \times 0.3$ mm^3 were kept after Ta-Li-Ta stack at a distance of 2.1 cm in forward direction. Aluminium (Al) foil of dimension $10 \times 10 \times 0.1$ mm was used as a flux monitor via ^{27}Al(n,α)^{24}Na reaction. To prevent radioactive contamination, the Nb and Sr samples were wrapped in 0.025 mm thick Al-foil. *Table 5.15* contains the samples and monitor details.

Table 5.15 Sample and monitor details used for experiments

Isotope	E_n (MeV)	Sample	Isotopic abundance (%)	Density (g/cm^3)	Weight (mg)	Number of target atoms (×10^{-4} atoms/b)
^{27}Al	13.97±0.68	Al-foil	100	2.7	27.97	6.243
	16.99±0.53				30.99	6.917
	20.02±0.58				31.3	6.986
^{88}Sr	13.97±0.68	Sr-foil	82.58	2.64	74.7	4.226
	16.99±0.53				76.9	4.354
^{93}Nb	13.97±0.68	Nb-foil	100	8.57	638.6	40.951
	20.02±0.58				701.8	45.494

Measurement of γ-ray activity

For offline γ-ray counting, the Al-Nb-Sr stack samples were exposed to 5-7 hours of proton beam radiation at 16, 19, and 22 MeV energies. This was done to ensure that the samples had enough activity. The target samples were cooled for an appropriate time following each irradiation, contingent on the half-life of the produced nuclides. After disassembling the stack, the individual irradiated samples were placed on various Perspex plates in preparation for offline γ-ray spectrometry. A pre-calibrated 80 cm^3 High Purity Germanium (HPGe) detector connected to a 4K multichannel analyzer running GENIE software on a personal computer was used to count the γ-rays emitted from the triggered target samples. The detector has the FWHM of 1.82 keV at 1332 keV γ-line of ^{60}Co. The samples were positioned appropriately away from the detector's end cap during γ-ray counting in order to prevent the pile-up effect and maintain the detector dead time less than 5%. To get accurate counting statistics and track the half-life of the target radionuclide, several γ-ray counts of each sample were performed over an increasing time period. The nuclear spectroscopic data of ^{93}Nb(n,2n)^{92}Nb^{m}, ^{88}Sr(n,2n)^{87}Sr^{m} reactions with ^{27}Al(n,α)^{24}Na monitor reaction are given in *Table 5.16* [36, 98, 99] and the typical γ-ray spectrum is shown in *Figure 5.12*.

Table 5.16 Nuclear spectroscopic data with uncertainties used in present experiments [24]

Reaction	Product	Half-life	Eγ (keV)	Iγ (%)
^{27}Al(n,α)	^{24}Na	14.997±0.012 hour	1368.626	99.9936±0.0015
^{93}Nb(n,2n)	^{92}Nb^{m}	10.15±0.02 day	934.44	99.15
^{88}Sr(n,2n)	^{87}Sr^{m}	2.815±0.012 hour	388.531	82.19±0.22

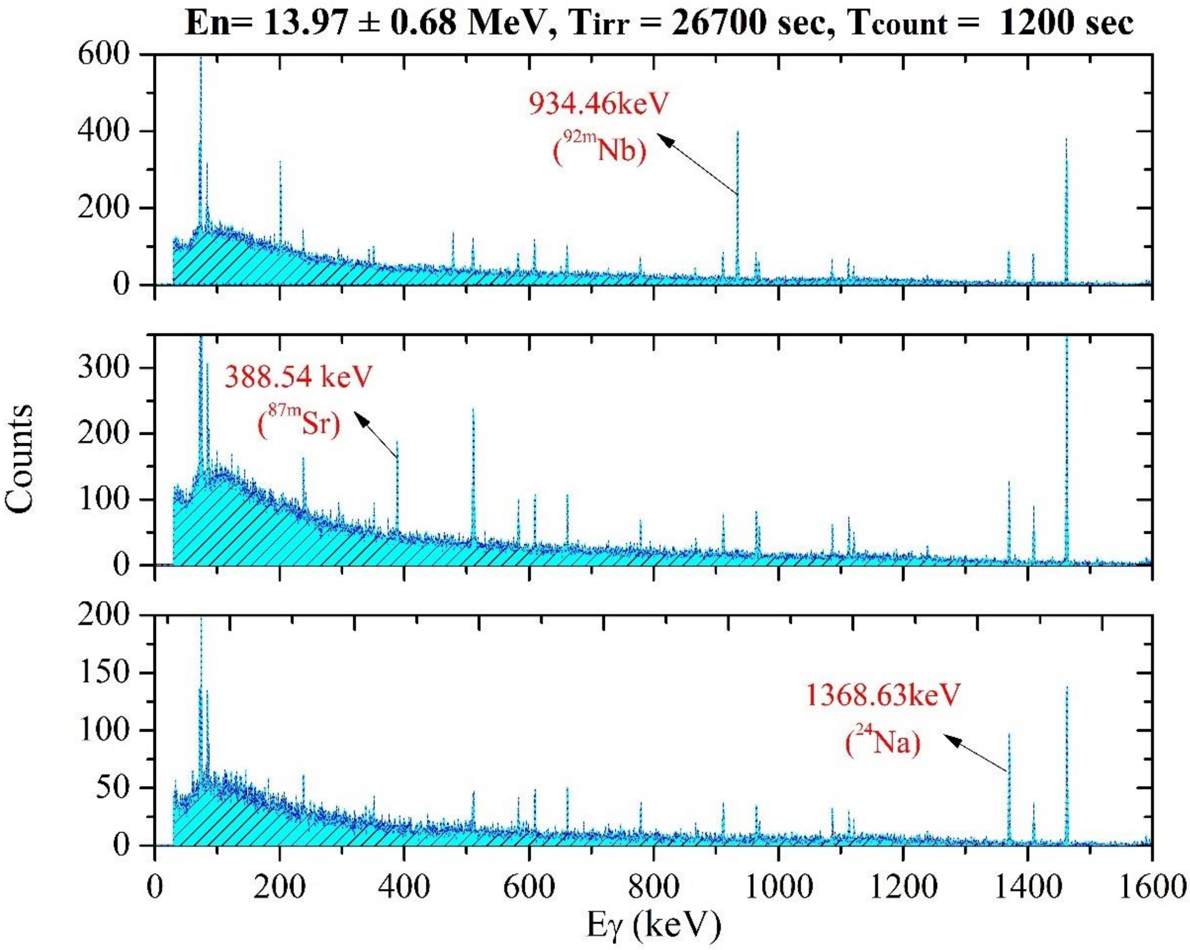

Figure 5.12 A typical γ-ray spectra of ^{93}Nb(n,2n)^{92}Nb^{m} , ^{88}Sr(n,2n)^{87}Sr^{m} and ^{27}Al(n,α)^{24}Na reactions for E_n = 13.97 ± 0.68 MeV recorded by HPGe detector

The same set of experiments as described in Section 5.3 were used to conduct the experiments for the niobium and strontium samples. Therefore, the HPGe detector's efficiency calibration and γ-ray activity measurement followed the same procedures as covered in the previous section.

Covariance analysis and uncertainty propagation in detector efficiency

The interpolation method, as discussed in Eq. (5.5), was used to determine the detector efficiency for ^{87m}Sr, ^{92m}Nb and ^{24}Na nuclides. The fitting parameters, provided in Eq. (5.7) were utilized for the efficiency calculations. The efficiency of the sample and monitor reactions with uncertainties and correlation matrix were calculated from the fitting parameters which are given in *Table 5.17*.

Table 5.17 Interpolated detection efficiencies with uncertainties and correlation matrices for the sample and monitor reactions

Reaction	Eγ (keV)	Efficiency	Correlations		
^{88}Sr(n,2n)^{87m}Sr	388.54	0.04714 ± 0.00097	1.		
^{93}Nb(n,2n)^{92m}Nb	934.46	0.02288 ± 0.00038	0.431	1.	
^{27}Al(n,α)^{24}Na	1368.625	0.01687 ± 0.00029	0.359	0.434	1.

Estimation of ^{93}Nb(n,2n)^{92m}Nb and ^{88}Sr(n,2n)^{87m}Sr reaction cross sections

Using the ratio technique, as outlined in Eq. (5.14) of Sub-Section 5.3.1, the averaged reaction cross section ($< \sigma_R >$) for the neutron spectrum was found for both reactions. *Table 5.16* contains the nuclear spectroscopic data used in these computations.

Correction factors

γ ray self-attenuation factor

In γ-ray spectroscopy method, the γ-rays from the nuclides make interactions within the sample due to self-attenuation effect. Therefore the correction factor for self-attenuation of γ-rays need to be determine when measuring cross sections using formula,

$$C_{attn} = \frac{\mu_m \rho d}{1-exp^{(-\mu_m \rho d)}} \tag{5.17}$$

Where, ρ and d is the sample density and thickness. μ_m is the mass attenuation coefficient calculated from the XMuDat version 1.0.1 [100].

Table 5.18 γ-ray self-attenuation correction and low energy background correction factors used to measure cross sections

Reaction	E_n	Eγ (keV)	$C_{attn.}$	N_{corr}
^{27}Al(n,α)^{24}Na	13.97±0.68	1368.626	1.00071	0.81309
	16.99±0.53			0.63229
	20.02±0.58			0.43170
^{88}Sr(n,2n)^{87}Sr^m	13.97±0.68	388.531	1.00397	1
	16.99±0.53			0.97818
^{93}Nb(n,2n)^{92}Nb^m	13.97±0.68	934.44	1.0190	0.92783
	20.02±0.58			0.69330

Low energy background correction

As discussed above, the proton energies for the irradiation are above the threshold energies of the first excited state of the ^{7}Li(p,n)^{7}Be reaction. Therefore contribution from the low energy background neutrons from ^{7}Li(p,n$_1$)^{7}Be* reactions needs to be subtract to determine the correct cross sections. Hence, the correction factor due to low energy background neutron is calculated by,

$$N_{corr} = 1 - \frac{\int_{E_{low}}^{E_{high}} \Phi_1(E)\sigma_x(E)dE}{\int_{E_{low}}^{E_{high}} \Phi(E)\sigma_x(E)dE} \tag{5.18}$$

Where, $\Phi_1(E)$ is the neutron flux energy spectrum for (p,n$_1$) neutrons and $\Phi(E) = \Phi_0(E) + \Phi_1(E)$ $\sigma_x(E)$ is the cross section values of sample reactions taken from JENDL-5 [16] and ^{27}Al(n,α)^{24}Na reaction cross section values taken from IRDFF-1.05 data library [101]. The calculated values of low energy corrections and the γ-ray self-attenuation correction factors of associated γ-ray energies of sample and monitor reactions are given in *Table 5.18*.

Reference monitor reaction cross section

Eq. (5.10) was used to measure the spectrum averaged monitor reaction cross section. The neutron flux spectrum displayed in *Figure 5.2* was folded with the ^{27}Al(n,α)^{24}Na reaction cross section retrieved from IRDFF-1.05 [101]. *Table 5.19* provides the spectrum averaged monitor cross section with uncertainties and correlation matrix for nearest point energies.

Table 5.19 $^{27}Al(n,\alpha)^{24}Na$ reaction cross section with uncertainties and correlation matrices

<En> (MeV)	Cross section $< \sigma_m >$ (mb)	$\Delta\ \sigma_m$ (%)	Correlations		
13.97 ± 0.68	122.54 ± 1.2621	1.03	1.		
16.99 ± 0.53	76.46 ± 0.3822	0.49	0.2509	1.	
20.02 ± 0.58	38.06 ± 0.4187	1.10	0.0128	0.1863	1.

Covariance analysis and uncertainty propagation in the reaction cross section

The fractional partial uncertainties propagate from various attributes involved in Eq. (5.14), such as photo-peak counts ($C_{s,m}$), spectrum averaged monitor cross section (σ_m), detector efficiency (η), γ-ray intensity ($I_{s,m}$), weight of samples ($W_{s,m}$), and timing factor ($f_{s,m}$). These factors were taken into consideration when determining the uncertainties in the measured cross sections of the ^{92m}Nb and ^{87m}Sr isotopes. Since the isotopic abundance of ^{93}Nb and ^{27}Al is 100%, the uncertainty resulting from this was not taken into account. *Table 5.20* provides the fractional partial uncertainty of the various attributes. The uncertainty in the neutron energies is estimated within 3%-5%. The uncertainty in the cross sections was estimated about 5% for ^{93}Nb(n,2n)^{92m}Nb reaction and about 6%-7% for ^{88}Sr(n,2n)^{87m}Sr reaction. The cross section with uncertainty and correlation matrix for the ^{93}Nb(n,2n)^{92m}Nb and ^{88}Sr(n,2n)^{87m}Sr reaction was given in *Table 5.21*.

Table 5.20 Partial uncertainties (%) of the ^{93}Nb(n,2n)^{92m}Nb and ^{88}Sr(n,2n)^{87m}Sr cross section due to different attributes in present experiment

Attributes		E_n = 13.97 ± 0.68 MeV	E_n = 16.99 ± 0.53 MeV	E_n = 20.02 ± 0.58 MeV
Counts	Nb	0.49955	-	1.47569
	Sr	0.0786	0.5341	-
	Al	3.1101	2.8917	1.2321
Weight	Nb	0.01566	-	0.01425
	Sr	0.13385	0.12992	-
	Al	0.3575	0.3227	0.3195
Intensity	Nb	0.01009	-	0.01009
	Sr	0.26767	0.26767	-
	Al	0.0015	0.0015	0.0015
Half-life	Nb	0.19704	0.19704	0.19704
	Sr	0.42629	0.42629	0.42629
	Al	0.08002	0.08002	0.08002
Efficiency	Nb	2.78571	-	2.78571
	Sr	2.22120	2.22120	-
	Al	1.70238	1.70238	1.70238
Monitor cross section	$\sigma_{m\text{-}Al}$	0.48148	0.81091	1.3189
Total	Nb	5.0029	-	5.2114
	Sr	6.2254	6.9369	-

Table 5.21 The measured $^{93}Nb(n,2n)^{92m}Nb$ and $^{88}Sr(n,2n)^{87m}Sr$ reaction cross section data with uncertainties and correlation matrices

<table>
<tr><th colspan="4">^{93}Nb(n,2n)^{92m}Nb reaction cross section (barn)</th></tr>
<tr><th>En (MeV)</th><th>Cross section (barn)</th><th colspan="2">Correlations</th></tr>
<tr><td>13.97 ± 0.68</td><td>0.39875 ± 0.01983</td><td>1.</td><td></td></tr>
<tr><td>20.02 ± 0.58</td><td>0.2166 ± 0.01126</td><td>0.5798</td><td>1.</td></tr>
<tr><th colspan="4">^{88}Sr(n,2n)^{87m}Sr reaction cross section (barn)</th></tr>
<tr><td>13.97 ± 0.68</td><td>0.24562 ± 0.01545</td><td>1.</td><td></td></tr>
<tr><td>16.99 ± 0.53</td><td>0.25387 ± 0.01765</td><td>0.3336</td><td>1.</td></tr>
</table>

5.4.2 Theoretical Calculations

TALYS is a software used to analyze and predict nuclear reaction cross sections induced by neutrons, photons, protons, deuterons, tritons, ^{3}He- and alpha-particles in the energy range of 1 keV to 200 MeV energy range and for target nuclides of mass 12 and heavier [8, 45]. The calculations are performed by ECIS06 code [58, 59]. The TALYS-1.9 code is now being used to calculate the reaction cross sections for ^{93}Nb(n,2n)^{92m}Nb and ^{88}Sr(n,2n)^{87m}Sr by taking into account default nuclear reaction models and different level density models (LD-models) between 13.97 and 20.02 MeV neutron energy. The TALYS-1.9 code offers six distinct level density models: The constant temperature model (CTM) at low energies and Fermi gas model at high energies [50], the Back-shifted Fermi gas level density model (BFM) [51], the Generalized Super-fluid Model (GSM) [52, 53] and the models of microscopic level densities [54, 55]. The comparison of present results with predicted cross sections for ^{93}Nb(n,2n)^{92}Nb^m reaction was presented in *Figure 5.13* for 10 to 24 MeV neutron energy and 12 to 20 MeV for ^{88}Sr(n,2n)^{87}Sr^m reaction as presented in *Figure 5.14*. The cross sections determined using various level density models for both the reactions have significant differences which shows in *Table 5.22* and *5.23* at interested neutron energies.

5.4.3 Results and Discussion

The experimental reaction cross sections from this work along with previously measured data, the available evaluated data from TENDL-2019, JENDL/AD-2017 and JEFF-3.3 and predicated data by TALYS-19 are shown in *Figure 5.13* and *5.14*. *Table 5.22* shows the comparison of ^{93}Nb(n,2n)^{92m}Nb reaction cross sections measured at 13.97 ± 0.68 MeV and 20.02 ± 0.58 MeV neutron energies. The predicated data from TALYS-1.9 overestimate the present data at 13.97 ± 0.68 MeV by about ~14% to 20% for LD-1 to LD-3 models and ~ 6% to 12% for LD-4 to LD-6 models while the evaluated data from TENDL-2019, JENDL/AD-2017 and JEFF-3.3 libraries overestimate the present data by ~11%-13% at 13.97 ± 0.68 MeV. For 20.02 ± 0.58 MeV, the predicated data over estimated the present data by ~11% to 27% for LD-1 to LD-6 models and the evaluated data overestimate the present data by ~31-33%.

Table 5.23 shows the comparison of ^{88}Sr(n,2n)^{87m}Sr reaction cross section at 13.97 ± 0.68 MeV and 16.99 ± 0.53 MeV energies. The predicated data from TALYS-1.9 underestimate the present data by 17% to 30% for LD-2 to LD-6 models and ~8% for LD-1 model while the evaluated data from TENDL-2019, JENDL/AD-2017 and JEFF-3.3 libraries underestimate the present data by ~17%-21% at 13.97 ± 0.68 MeV. For 16.99 ± 0.53 MeV, the predicated data overestimate by ~9% -12% for LD-1 and LD-2 model and ~0.7%-5% for LD-3 to LD-6 models. The evaluated data overestimate the present data by ~0.1-3% at 16.99 ± 0.53 MeV.

Table 5.22 Comparison of $^{93}Nb(n,2n)^{92m}Nb$ reaction cross section

E_n (MeV)	Cross section (barn).									
	Measured	LD-1	LD-2	LD-3	LD-4	LD-5	LD-6	TENDL-	JENDL/AD-	JEFF-3.3
13.97±0.68	0.39875±0.01983	0.51688	0.49607	0.46571	0.43454	0.42568	0.35075	0.45902	0.44799	0.45903
20.02±0.58	0.21660±0.01126	0.28575	0.30573	0.29876	0.26342	0.25953	0.24358	0.32254	0.31928	0.32272

Table 5.23 Comparison of $^{88}Sr(n,2n)^{87m}Sr$ reaction cross section

E_n (MeV	Cross section (barn)									
	Measured	LD-1	LD-2	LD-3	LD-4	LD-5	LD-6	TENDL-2019	JENDL/AD-2017	JEFF-3.3
13.97±0.68	0.24562±0.01545	0.22484	0.20274	0.16903	0.21893	0.20078	0.18975	0.19200	0.20216	0.19647
16.99±0.53	0.25387±0.01765	0.28956	0.28103	0.25000	0.25914	0.24116	0.25214	0.26200	0.25420	0.26276

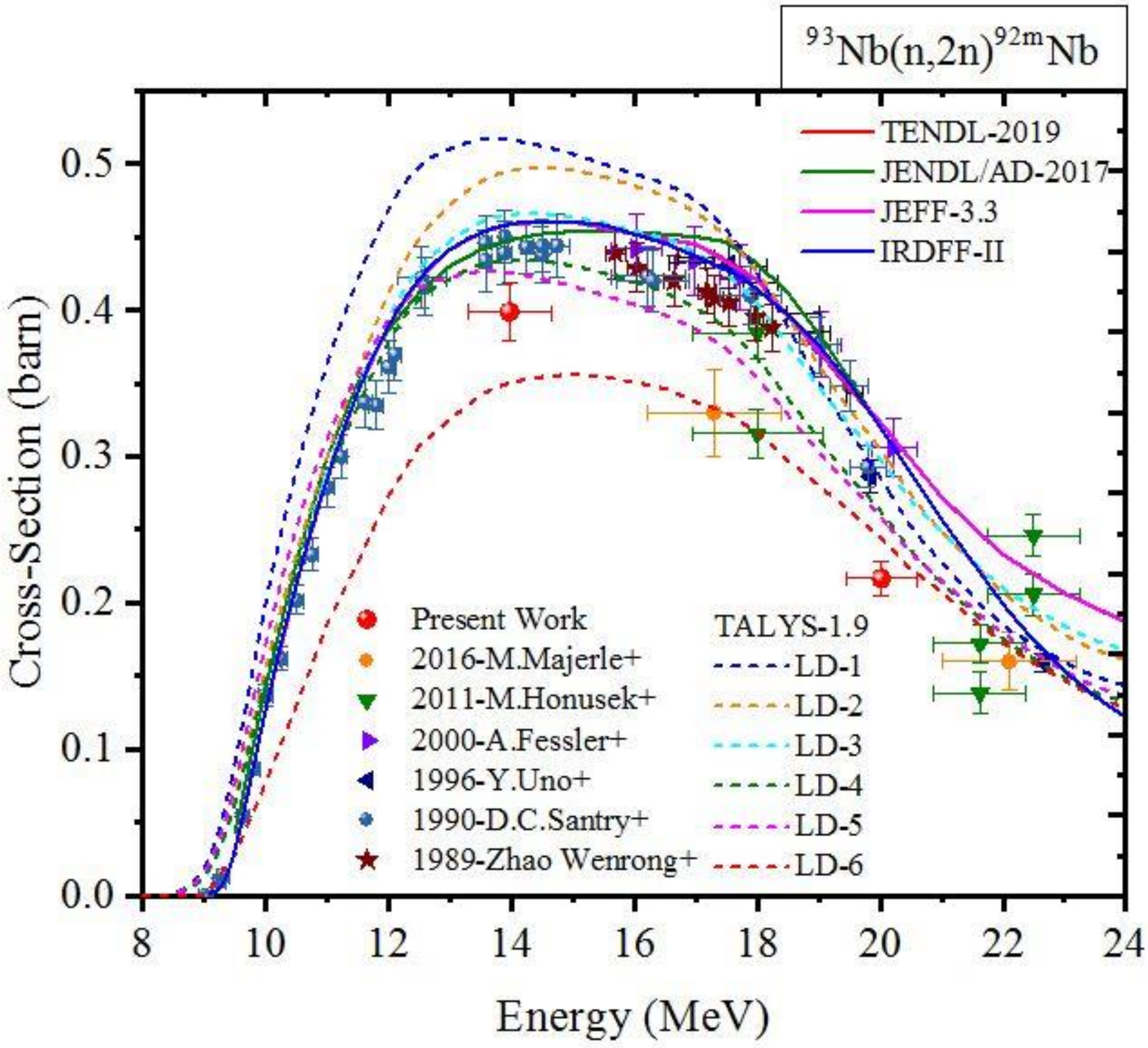

Figure 5.13 Comparison of ^{93}Nb(n,2n)^{92m}Nb reaction cross section with the previously published data, evaluated data and predicated data by TALYS-1.9 code

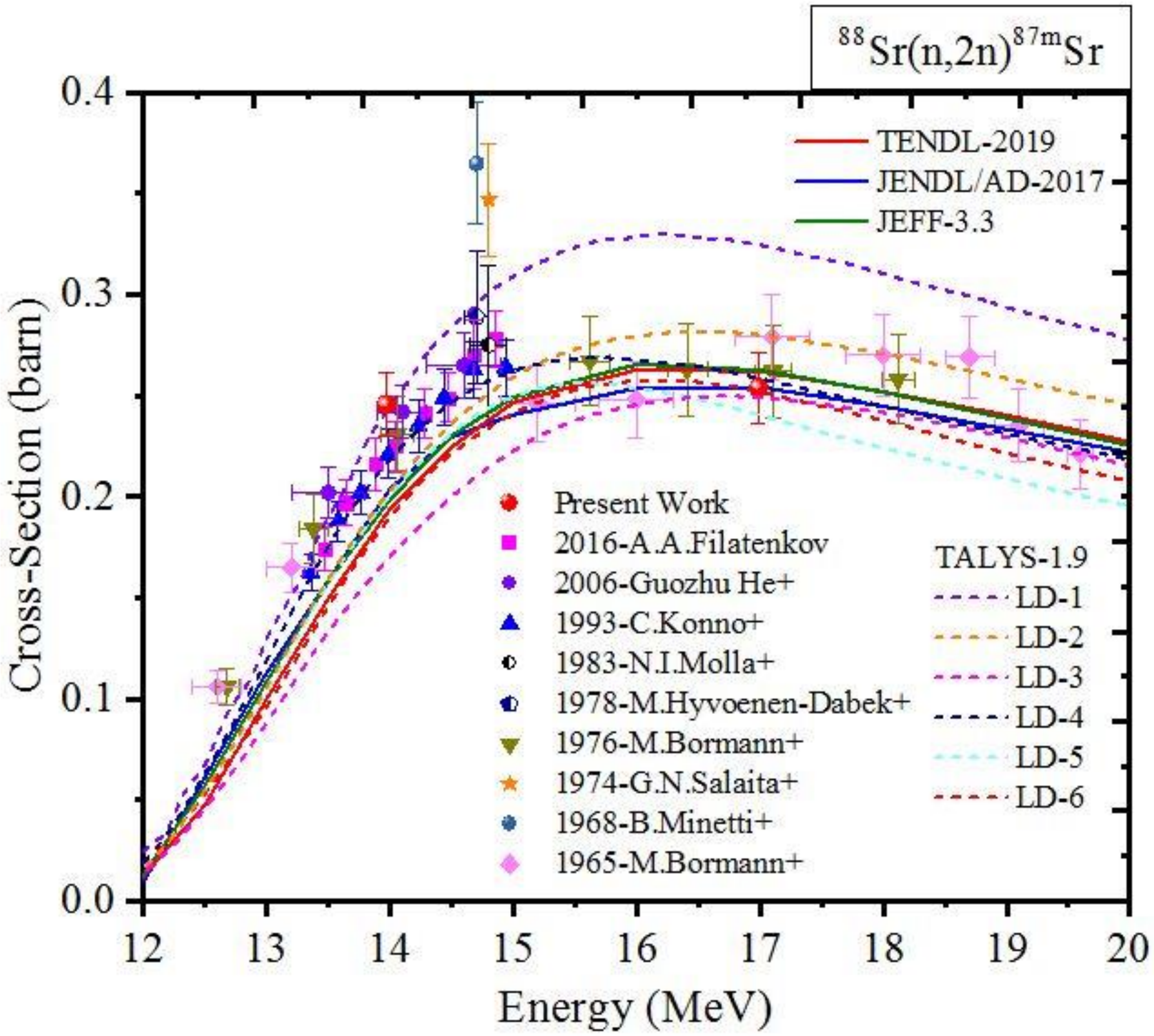

Figure 5.14 Comparison of ^{88}Sr(n,2n)^{87m}Sr reaction cross section with the previously published data, evaluated data and predicated data by TALYS-1.9 code

5.5 Cross section of ^{85}Rb(n,p)^{85m}Kr and ^{85}Rb(n,2n)^{84m}Rb reactions

As described in Chapter 1, the precise understanding of neutron activation cross sections is essential for comprehension and appropriate material selection in nuclear technology applications and nuclear theory research. [102], neutron activation analysis, isotope production, medical technology and others. In this section, the cross section measurement has been carried out for rubidium isotope for the reasons as follows: (i) K. Heyde et al. [103] reported in their theoretical studies that for the nuclei lie between the magic numbers of 28 and 50, shape coexistence plays a prominent role in their structure. (ii) Otuka et al. [6] reported in their theoretical work that many kinds of cross sections have been measured and published but users encounter challenges because of significant inconsistencies and a deficiency of information regarding measurement uncertainties. For both reactions, several cross section values were reported in the EXFOR database [7], but no report containing a thorough characterization of uncertainties using the covariance analysis approach could be located. In the neutron energy range of 12 to 20 MeV, the goal of the current work is to measure the cross section of the ^{85}Rb(n,2n)^{84m}Rb and ^{85}Rb(n,p)^{85m}Kr reactions. The cross section data will be reported with uncertainties propagating from all attributes involved in the activation equation as well as covariance and correlation matrix. The nuclear reaction model code TALYS-1.96 [8] has been used to compute the cross section. The measured cross section values are compared with the data from the published literature and the JENDL-5 and EAF 2010 library evaluations [16, 17].

5.5.1 Data Analysis

In the present experiment, rubidium sample was in the form of pellet while aluminum was utilized as a thin metal foil of thickness 0.1 mm. A $RbNo_3$ powder form of known amount was utilized to prepare circular pellet of diameter 1 cm packed into the polyethylene bag. The absolute neutron flux was calculated using the ^{27}Al(n,α)^{24}Na reaction. The reference monitor cross section was taken from the standard IRDFF-II data library [104]. The sample details are given in *Table 5.24*. The sample weight measurements were performed using the AFCOSET ER-182A manufacture micro balance, which has the lowest count of 0.1 mg. The "Rb-Al" stack with the samples for irradiation oriented 0° to the beam direction.

Table 5.24 Sample and monitor details used in the present experiment

Sample	Isotope	Isotopic abundance (%)	Density (g/cm^3)	E_n (MeV)	Weight (gm)	Number of target atoms (×10^{-4} atoms/b)
Al-foil	^{27}Al	100	2.7	12.97 ± 0.51	0.0125	2.789
				15.72 ± 0.60	0.0134	2.991
				16.73 ± 0.66	0.0125	2.789
				18.99 ± 0.74	0.0134	2.991
$RbNo_3$ powder	^{85}Rb	72.17	1.532	12.97 ± 0.51	0.3007	15.29
				15.72 ± 0.60	0.3017	15.34
				16.73 ± 0.66	0.3007	15.29
				18.99 ± 0.74	0.2996	15.24

Measurement of γ-ray activity

The irradiations of the samples were carried out for sufficient time to produce enough activity in the samples. After stopping the irradiations and sufficient cooling times, the samples were transferred to the counting room. The target sample and the monitor sample were mounted on the Perspex plate and taken for the offline γ-ray spectroscopy. The emitted γ-rays from the product nuclides (^{84m}Rb, ^{85m}Kr and ^{24}Na) were recorded by a pre-calibrated 80 cm^3 high purity germanium (HPGe) detector having 40% relative efficiency and a 1.82 keV energy resolution at 1332.50 keV γ-energy of ^{60}Co. The detector was coupled with a PC-based 4096 channel analyzer with CMAC based Linux Advanced Multi-Parameter System LAMPS software and the dead time of the detector was <5% throughout the counting time. The nuclear spectroscopic data with uncertainties of the sample and monitor reactions are given in *Table 5.25* [105-107]. A typical γ-ray spectrum recorded by HPGe detector for ^{84m}Rb and ^{85m}Kr nuclides is presented in *Figure 5.15*.

Table 5.25 Nuclear spectroscopic data with uncertainties used in present experiment

Reaction	Product	Half-life	Eγ (keV)	Iγ (%)
^{85}Rb(n,2n)	^{84m}Rb	20.26 ± 0.04 (min)	463.62	33.1 ± 0.24
^{85}Rb(n,p)	^{85m}Kr	4.408 ± 0.008 (hour)	151.195	75.5 ± 0.5
^{27}Al(n,α)	^{24}Na	14.997 ± 0.012 (hour)	1368.625	99.9940 ± 0.0020

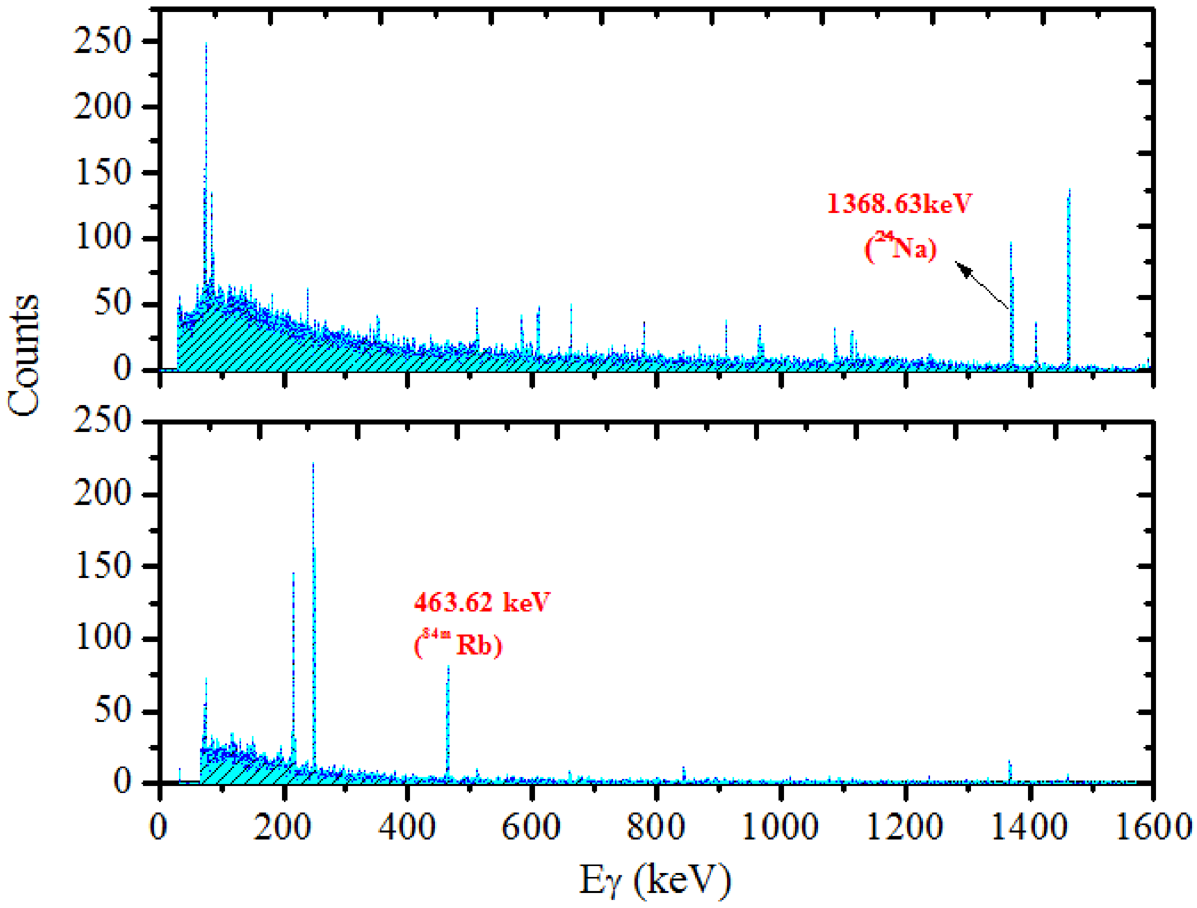

Figure 5.15 A typical γ-ray spectra of ^{85}*Rb(n,2n)*^{84m}*Rb,* ^{85}*Rb(n,p)*^{85m}*Kr and* ^{27}*Al(n,α)*^{24}*Na reactions for* $E_n = 18.99 \pm 0.74$ *MeV recorded by HPGe detector*

Using a reference ^{152}Eu source ($\tau_{1/2}$ = 13.517 ± 0.009 year) with known activity (A_0 = 7767.73 ± 88.1 Bq as of 1-October-1999), the efficiency calibration of the HPGe detector was measured for various γ-ray energies [40]. Using the relations, the HPGe detector efficiency was calculated,

$$\varepsilon = \frac{C_{obs}K_c}{A_o I_\gamma e^{-\lambda T}\, \nabla t} \tag{5.19}$$

Where, C_{obs} is the photo peak counts measured in time (Δt = 3754 sec), A_0 is the ^{152}Eu-source activity at the time of manufacturing, I_γ is the γ-ray intensity, T is the time interval between the source manufacturing to the experiment date. K_c is the coincidence summing correction factor. The irradiated samples were kept at a distance of 3 mm from the detector end cap, the correction for the coincidence summing effects of γ-ray energy lines was made in the detector efficiency measurements. The Monte Carlo simulation code EFFTRAN [41] was used to calculate the correction factor (K_c). The code required the material and dimension details of the crystal, cavity, housing, window and mounting holder of the HPGe detector and calibration source [42-43]. The measured efficiency is given in *Table 5.26* and the comparison of measured efficiency with the EFFTRAN code is presented in *Figure 5.16*.

Table 5.26 HPGe detector efficiency with summing correction factors

Eγ (keV)	$I\gamma$	Counts (C_{obs})	K_c	Efficiency	Efficiency with K_c
121.78	0.2853 ± 0.0016	323969 ± 2591	1.104	0.1075	0.1187
244.69	0.0755 ± 0.0004	49039 ± 619	1.138	0.0615	0.0700
443.96	0.0282±0.00014	12260 ± 195	1.058	0.0372	0.0393
964.079	0.1451 ± 0.0007	33819 ± 405	1.058	0.0221	0.0234
1112.07	0.1367 ± 0.0008	26606 ± 345	1.025	0.0184	0.0189
1408.006	0.2087 ± 0.0009	33200 ± 364	1.04	0.0151	0.0157

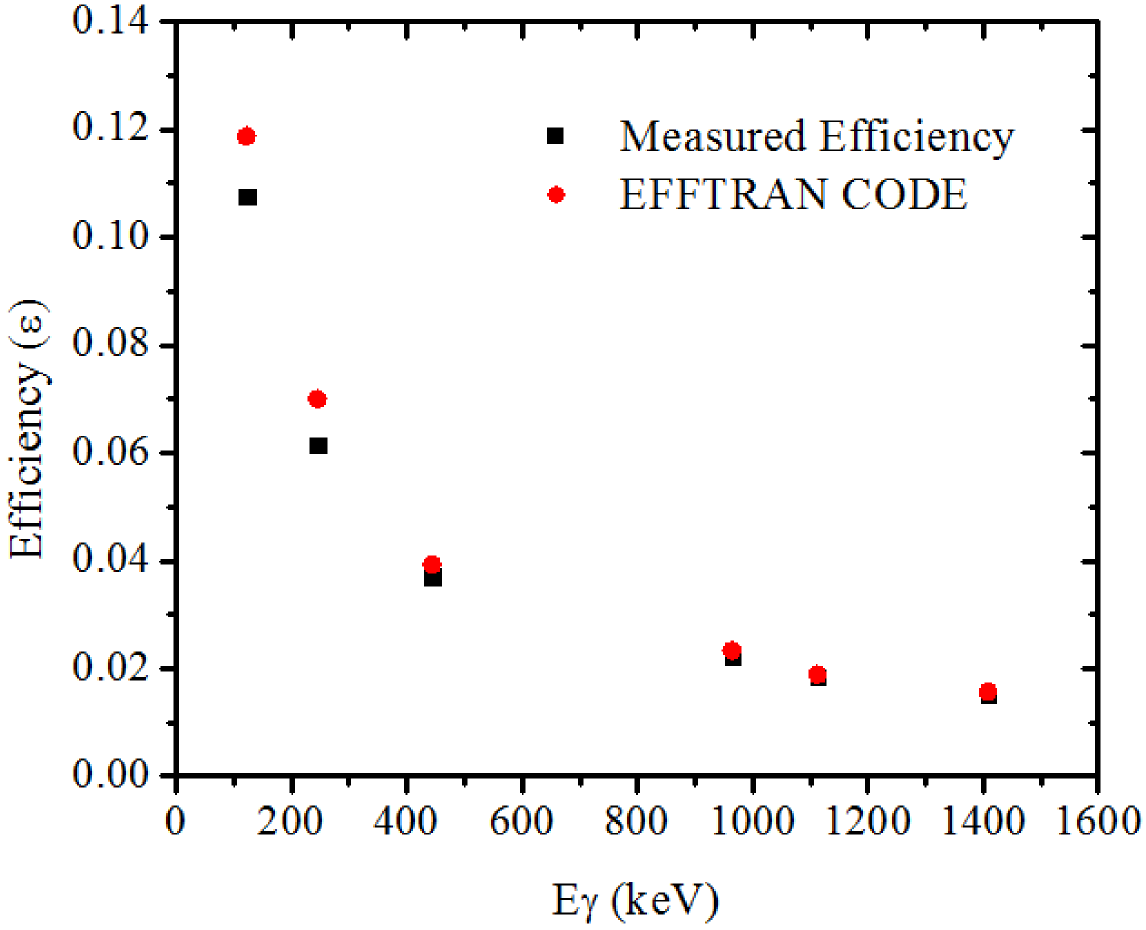

Figure 5.16 Comparison of measured efficiency with EFFTRAN Code corrected efficiency

Covariance analysis and uncertainty propagation in detector efficiency

The covariance matrix for the detector efficiency was determined which gives the complete information of the uncertainties in the measurements. From Eq. (5.19), the efficiency is the function of counts, γ-ray intensity, activity and the decay constant. In the measured efficiency the uncertainties propagate from these four attributes $\varepsilon = \Delta\varepsilon\,(\Delta C_{obs}, \Delta I_{\gamma}, \Delta A_0, \Delta T_{1/2})$. Therefore the total uncertainties were calculated using the formula,

$$\left(\frac{\Delta\varepsilon_i}{\varepsilon_i}\right)^2 = \left(\frac{\Delta C_i}{C_i}\right)^2 + \left(\frac{\Delta A_0}{A_0}\right)^2 + \left(\frac{\Delta I_{\gamma i}}{I_{\gamma i}}\right)^2 + (t\Delta\lambda)^2 \qquad (5.20)$$

Where, ΔC_i, A_0 and $\Delta I_{\gamma i}$ are the uncertainties in counts, source activity and the γ-ray intensities respectively, and $\Delta\lambda = 0.693 \times \Delta T_{1/2}/T_{1/2}^2$ is the uncertainty in the decay constant. The partial uncertainties values of all four attributes are important to create the covariance matrix for the detector efficiencies which is determined by,

$$(V_\varepsilon)_{ij} = \sum_r e_{ir} S_{ijr} e_{jr} \tag{5.21}$$

Where, e_{ir} and e_{jr} are the n × n diagonal matrices and S_{ijr} are the n × n micro-correlation matrix. The partial uncertainties of the attributes are given in *Table 5.27*. The covariance matrix and the correlation matrices for the HPGe detection efficiency are presented in *Table 5.28*. The total error in the measured efficiency is the variance of the diagonal covariance matrix given by $(\sigma_\varepsilon)_{ii} = ((V_\varepsilon)_{ii})^{1/2}$ [108].

Table 5.27 Partial Uncertainties of parameters to obtain HPGe detector efficiency

Eγ (keV)	Iγ	Counts (C_{obs})	Half-life ($T_{1/2}$)	Activity (A_0)
121.78	6.031×10^{-4}	8.602×10^{-4}	7.161×10^{-5}	1.220×10^{-3}
244.69	3.259×10^{-4}	7.765×10^{-4}	34.096×10^{-5}	6.980×10^{-4}
443.96	1.845×10^{-4}	5.934×10^{-4}	2.474×10^{-5}	4.216×10^{-4}
964.079	1.065×10^{-4}	2.648×10^{-4}	1.470×10^{-5}	2.505×10^{-4}
1112.07	1.079×10^{-4}	2.393×10^{-4}	1.227×10^{-5}	2.092×10^{-4}
1408.006	6.497×10^{-5}	1.655×10^{-4}	1.003×10^{-5}	1.710×10^{-4}

Table 5.28 Covariance and Correlation matrices for HPGe detector efficiency

Eγ (keV)	Covariance matrix (× 10^{-7})						Correlations					
121.78	25.97						1.					
244.69	8.545	11.98					0.484	1.				
443.96	5.161	2.953	5.645				0.426	0.359	1.			
964.079	3.067	1.755	1.059	1.442			0.501	0.422	0.371	1.		
1112.07	2.561	1.465	0.885	0.526	1.131		0.474	0.398	0.350	0.412	1.	
1408.006	2.093	1.197	0.723	0.429	0.358	0.609	0.526	0.443	0.390	0.458	0.432	1.

The detector efficiency of γ-ray energies from ^{84m}Rb, ^{85m}Kr and ^{24}Na nuclides was determined by the interpolation method through the linear parametric function [23, 24],

$$\ln(\varepsilon_i) = \sum_m P_m \ (\ln E_i)^{m-1} \tag{5.22}$$

Where, P_m is the fitting parameter, ε_i and E_i is the efficiency and corresponding γ-ray energy of ^{152}Eu source. The above Eq. (5.22) can be written as Z = AP, with fitting parameters P_m and the corresponding covariance matrix V_p, is given as,

$$P_m = V_p \, (A^T V_Z^{-1} A) \, ; V_p = \ (A^T V_Z^{-1} Z) \tag{5.23}$$

Where, V_z matrix can be obtained as, $V_Z = \left(V_{\varepsilon_{ij}}\right) / < \varepsilon_i >< \varepsilon_j >$

The goodness of the fit can be obtained as,

$$\chi_m^2 = (Z - AP)' V_Z^{-1} (Z - AP) \tag{5.24}$$

By using the above definitions, the fitting parameters for the detector efficiencies of sample and monitor reaction residues γ-rays were found to be,

$$P_m = (-3.90622, -0.746071, 0.116215, -0.024697, -0.027535) \ ; \ \ \chi_m^2 = 2.29$$

From the above fitting parameters, the fitted efficiency curve and the measured efficiency are shown in *Figure 5.17*. The calculated detector efficiencies with uncertainties for ^{84m}Rb, ^{85m}Kr and ^{24}Na nuclides and corresponding correlation matrix are given in *Table 5.29*.

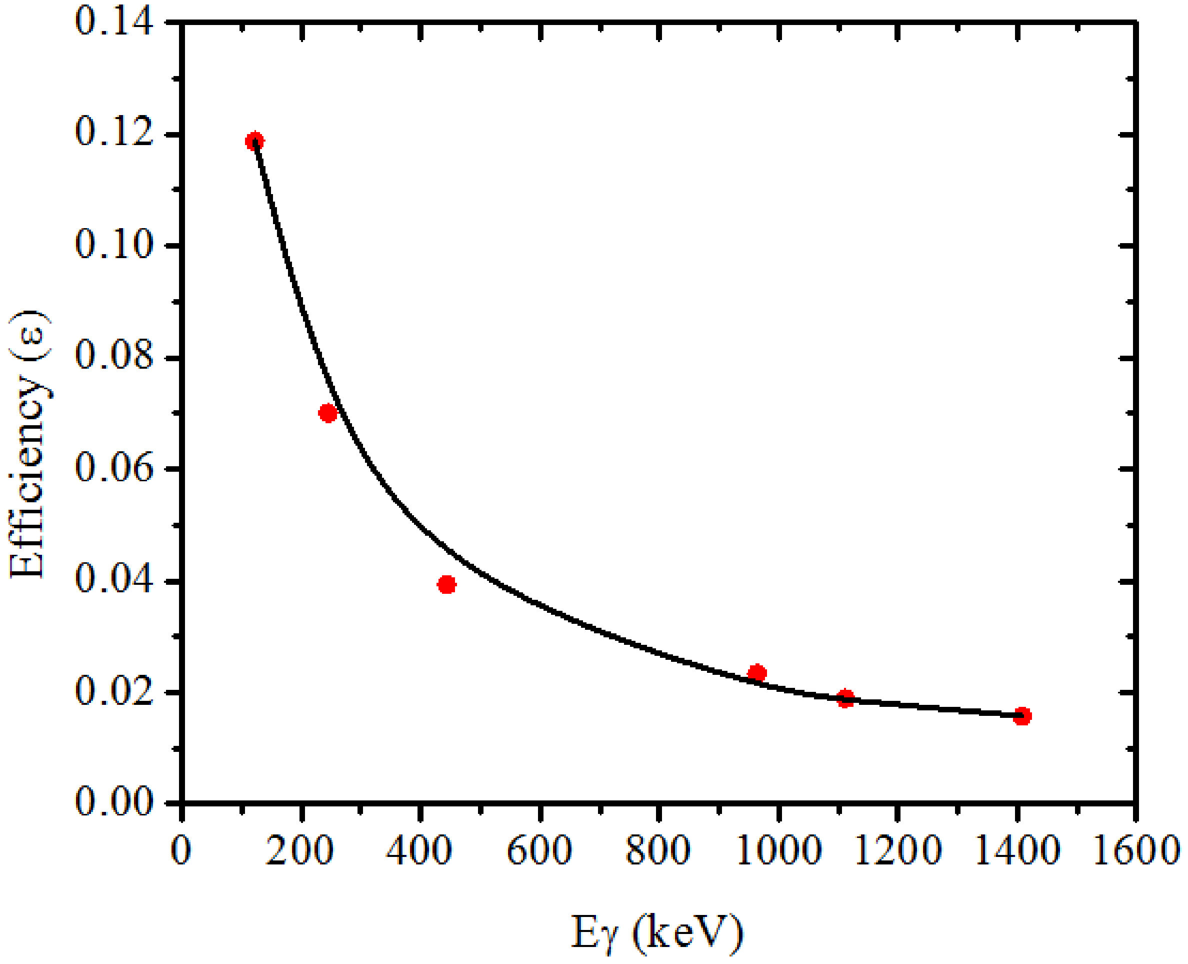

Figure 5.17 Plots of Efficiency fitted and the measured efficiency

Table 5.29 Interpolated detection efficiencies with uncertainties and correlation matrices for sample and monitor reactions

Reaction	Eγ (keV)	Efficiency	Correlations		
^{85}Rb(n,p)^{85m}Kr	151.195	0.10371 ± 0.00172	1.		
^{85}Rb(n,2n)^{84m}Rb	463.62	0.03829 ± 0.00071	0.237	1.	
^{27}Al(n,α)^{24}Na	1368.625	0.01608 ± 0.00024	0.579	0.376	1.

Estimation of ^{85}Rn(n,p)^{85m}Kr and ^{85}Rb(n,2n)^{84m}Rb reactions cross section

The neutron averaged spectrum average cross section ($<\sigma_r>$) for both reactions were measured relative to ^{27}Al(n,α)^{24}Na reference monitor reaction cross sections ($<\sigma_m>$) using standard activation formula as,

$$<\sigma_r> = <\sigma_m> \eta \, \frac{A_r\lambda_r a_m N_m I_m f_m}{A_m\lambda_m a_r N_r I_r f_r} \times \frac{C_{attn(r)} * N_{Corr\,(r)}}{C_{attn(m)} * N_{Corr\,(m)}} \tag{5.25}$$

Where, η ($\varepsilon_m/\varepsilon_r$) is the detector efficiency ratio, $\varepsilon_{r,m}$ is the efficiency of corresponding γ-ray energies of sample and monitor reaction, $A_{r,m}$ is the counts of photo-peak recorded by HPGe detector, $\lambda_{r,m}$ is the decay constant (cm^{-1}), $N_{r,m}$ is the total number of atoms, $I_{r,m}$ is the γ-ray intensity, $a_{r,m}$ is the isotopic abundance of the target and monitor nuclei. The nuclear spectroscopic data are given in *Table 5.24* and *5.25*. $f_{r,m}$ is the timing factors of the sample and monitor reaction are given by,

$$f_{r,m} = \left(1 - e^{-\lambda t_{irr}}\right) e^{-\lambda t_{cool}} \left(1 - e^{-\lambda t_{count}}\right) \tag{5.26}$$

Where, t_{irr} is the irradiation time, t_{cool} is the cooling time which is the time difference when the irradiation stop and the counting start time and t_{count} is the counting time. $C_{attn(r,m)}$ is γ-ray self-attenuation correction factor. $N_{corr\,(r,m)}$ is the low energy neutron correction factor.

Table 5.30 γ-ray self-attenuation correction and low energy background correction factors used to measure cross sections

Reaction	Eγ (keV)	Cattn.	En (MeV)	Ncorr
^{85}Rb(n,p)^{85m}Kr	151.195	1.0488 ± 0.00248	12.97 ± 0.51	0.8144
			15.72 ± 0.60	0.7711
			16.73 ± 0.66	0.7198
			18.99 ± 0.74	0.6907
^{85}Rb(n,2n)^{84m}Rb	463.62	1.01348 ± 0.00068	12.97 ± 0.51	-
			15.72 ± 0.60	0.9885
			16.73 ± 0.66	0.9429
			18.99 ± 0.74	0.8681
^{27}Al(n,α)^{24}Na	1368.625	1.00071 ± 0.00004	12.97 ± 0.51	0.8418
			15.72 ± 0.60	0.7267
			16.73 ± 0.66	0.6256
			18.99 ± 0.74	0.5144

Correction factors

In present measurements, the γ-ray self-attenuation correction factor and the low energy background neutron correction factors were calculated from the Eq. (5.17) and (5.18) discussed in Sub-Section 5.4.1. The calculated values of low energy corrections and the γ-ray self-attenuation correction factors of associated γ-ray energies of sample and monitor reactions are given in *Table 5.30*.

Reference monitor reaction cross section and its correlation matrix

In present work, the neutrons produced from ^{7}Li(p,n) reaction are not monoenergetic therefore the spectrum averaged monitor reaction cross section ($<\sigma_m>$) was calculated by,

$$< \sigma_m > = \frac{\int_{E_{low}}^{E_{high}} \Phi_0(E)\sigma_m(E)dE}{\int_{E_{low}}^{E_{high}} \Phi_0(E)dE} \tag{5.27}$$

Where, σ_m is the monitor ^{27}Al(n,α)^{24}Na monitor reaction cross section from IRDFF-II folded with the neutron flux spectrum shown in *Figure 5.15*. The spectrum averaged monitor cross section at nearest point energies with uncertainties and the correlation matrix is given in *Table 5.31*.

Table 5.31 ^{27}Al(n,α)^{24}Na reaction cross section with uncertainties and correlation matrices

<En> (MeV)	Cross section $< \sigma_m >$ (mb)	Δ σ_m (%)	Correlations			
12.97 ± 0.51	123.64 ± 1.280	1.04	1.			
15.72 ± 0.60	96.91 ± 0.4846	0.50	0.0731	1.		
16.73 ± 0.66	80.69 ± 0.5245	0.65	0.1436	0.8022	1.	
18.99 ± 0.74	48.63 ± 0.5350	1.10	0.6699	0.0389	0.4024	1.

Covariance analysis and uncertainty propagation in cross section

Nuclear data with statistics are important for researcher for precise and accurate evaluation. As a result, the reported experimental data are important with uncertainties and covariance matrix. In present study, the ^{85}Rb(n,2n)^{84m}Rb and ^{85}Rb(n,p)^{85m}Kr reaction cross sections were measures at averaged neutron energies of 12.97 ± 0.51, 15.72 ± 0.60, 16.73 ± 0.66 and 18.99

± 0.74 MeV respectively. The cross section was measured by a ratio method. In the covariance analysis, the covariance matrix for the measured cross section was calculated by the formula,

$$(V_\sigma)_{ij} = \sum_r e_{ir} S_{ijr} e_{jr} \tag{5.28}$$

Where, e_{ir} and e_{jr} are the n × n diagonal matrices of the partial uncertainties of i^{th} and j^{th} attributes and S_{ijr} are the n × n micro-correlation matrix. The partial uncertainties of the various attributes such as monitor cross section ($<\sigma_m>$), γ-ray photo peak counts (A_s, A_m), efficiency ratio (η), γ-ray intensity (I_γ) and isotopic abundance of sample and monitor ,timing factor (f_s, f_m) and number of atoms (N_s, N_m) were used to calculate the uncertainties in the cross section. The partial uncertainties and the cross section with uncertainties and correlation matrix for ^{85}Rb(n,p)^{85m}Kr and ^{85}Rb(n,2n)^{84m}Rb reactions are presented in *Table 5.32* to *5.35*.

Table 5.32 Partial uncertainties of ^{85}Rb(n,p)^{85m}Kr reaction cross section measurements with respect to the ^{27}Al(n,α)^{24}Na monitor reaction

Parameters	**Partial Uncertainty (%)**				**Correlation**
	12.97 MeV	15.72 MeV	16.73 MeV	18.99 MeV	
A_S	5.018	3.841	4.573	3.848	0
A_m	6.057	5.395	3.554	5.431	0
I_s	0.6649	0.6649	0.6649	0.6649	1
I_m	0.0015	0.0015	0.0015	0.0015	1
f_s	0.0551	0.0318	0.0054	0.0451	1
f_m	0.0027	0.0057	0.0077	0.0014	0
W_s	0.0333	0.0331	0.0333	0.0334	0
W_m	0.8	0.7463	0.8	0.7463	0
σ_m	1.037	0.6	0.7499	1.10	1
a_s	0.0139	0.0139	0.0139	0.0139	1
C_{att-s}	0.236	0.236	0.236	0.236	1
C_{att-m}	0.004	0.004	0.004	0.004	1
$\eta_{m,s}$	1.026	1.026	1.026	1.026	1

Table 5.33 The measured ^{85}Rb(n,p)^{85m}Kr reaction cross section data with uncertainties and correlation matrices

En (MeV)	Cross section (barn)	Correlations			
12.97 ± 0.51	0.00431 ± 0.000348	1.			
15.72 ± 0.60	0.00538 ± 0.000365	0.0275	1.		
16.73 ± 0.66	0.00469± 0.000283	0.0310	0.0368	1.	
18.99 ± 0.74	0.00336± 0.000232	0.0270	0.0322	0.0362	1.

Table 5.34 Partial uncertainties of ^{85}Rb(n,2n)^{84m}Rb reaction cross section measurements with respect to the ^{27}Al(n,α)^{24}Na monitor reaction

Parameters	**Partial Uncertainty (%)**				**Correlation**
	En = 12.97 ± 0.51 MeV	En = 15.72 ± 0.60 MeV	En = 16.73 ± 0.66 MeV	En = 18.99 ± 0.74 MeV	
A_S	4.794	3.783	3.604	3.124	0
A_m	6.057	5.395	3.554	5.431	0
I_s	0.7251	0.7251	0.7251	0.7251	1
I_m	0.0015	0.0015	0.0015	0.0015	1
f_s	0.0654	0.0860	0.0889	0.0674	1
f_m	0.0027	0.0054	0.0077	0.0014	0
W_s	0.0333	0.0331	0.0333	0.0334	0
W_m	0.8	0.7463	0.8	0.7463	0
σ_m	1.037	0.6	0.7499	1.10	1
a_s	0.0139	0.0139	0.0139	0.0139	1
C_{att-s}	0.067	0.067	0.067	0.067	1
C_{att-m}	0.004	0.004	0.004	0.004	1
$\eta_{m,s}$	0.1569	0.1569	0.1569	0.1569	1

Table 5.35 The measured ^{85}Rb(n,2n)^{84m}Rb reaction cross section data with uncertainties and correlations matrices

En (MeV)	Cross section (barn)	Correlations			
12.97 ± 0.51	0.47476 ± 0.03735	1.			
15.72 ± 0.60	0.5806 ± 0.03889	0.0107	1.		
16.73 ± 0.66	0.6450± 0.03372	0.0137	0.0162	1.	
18.99 ± 0.74	0.6301± 0.04062	0.0111	0.0131	0.0167	1.

5.5.2 Theoretical Calculations

Theoretically, the ^{85}Rb(n,p)^{85m}Kr and ^{85}Rb(n,2n)^{84m}Rb reaction cross sections from threshold to 20 MeV neutron energies were calculated using TALY-1.96 code [8]. In the present study, the input parameters were used as a default only the level density models were taken for the cross section measurements. There are six level density models are present for the selections as follows: (i) ldmodel 1 (Constant and Fermi-gas model); (ii) ldmodel 2 (Back-shifted Fermi-gas model); (iii) ldmodel 3 (Generalized super-fluid model); (iv) ldmodel 4 (microscopic level densities from (Skyrme force) Goriely's tables) [44]; (v) ldmodel 5 (microscopic level densities Skyrme force) from Hilaire's combinatorial tables) [44]; and (vi) ldmodel 6 (microscopic level densities -temperature dependent HFB, Gogny force) from Hilaire's combinatorial tables) [44]. The cross section for both the reactions was compared with the measured cross section values, available published data and also with the evaluated data from JENDL 5and EAF 2010 data in *Figure 5.18* and *5.19*.

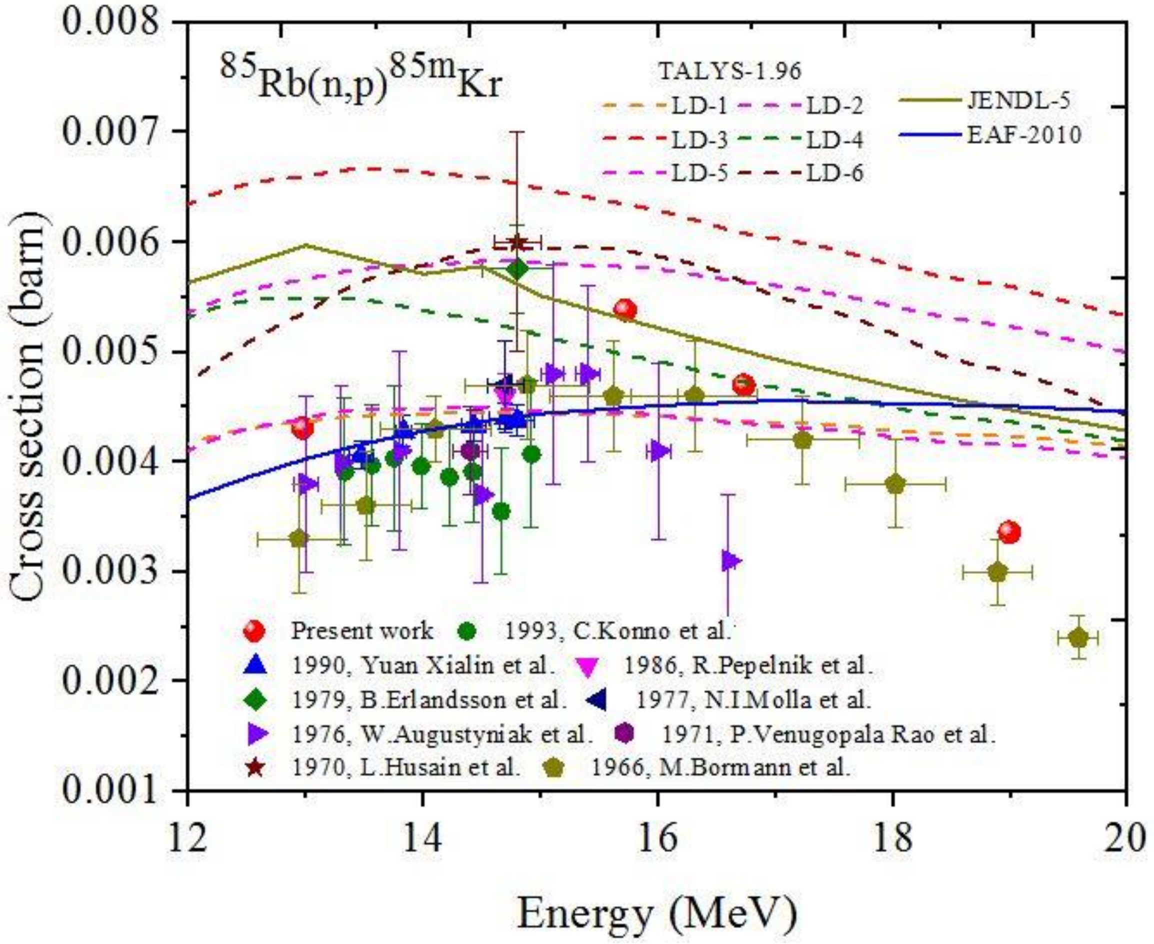

Figure 5.18 Comparison of ^{85}Rb(n,p)^{85m}Kr reaction cross section with reported data, theoretically calculated data by TALYS-1.96 and evaluated data

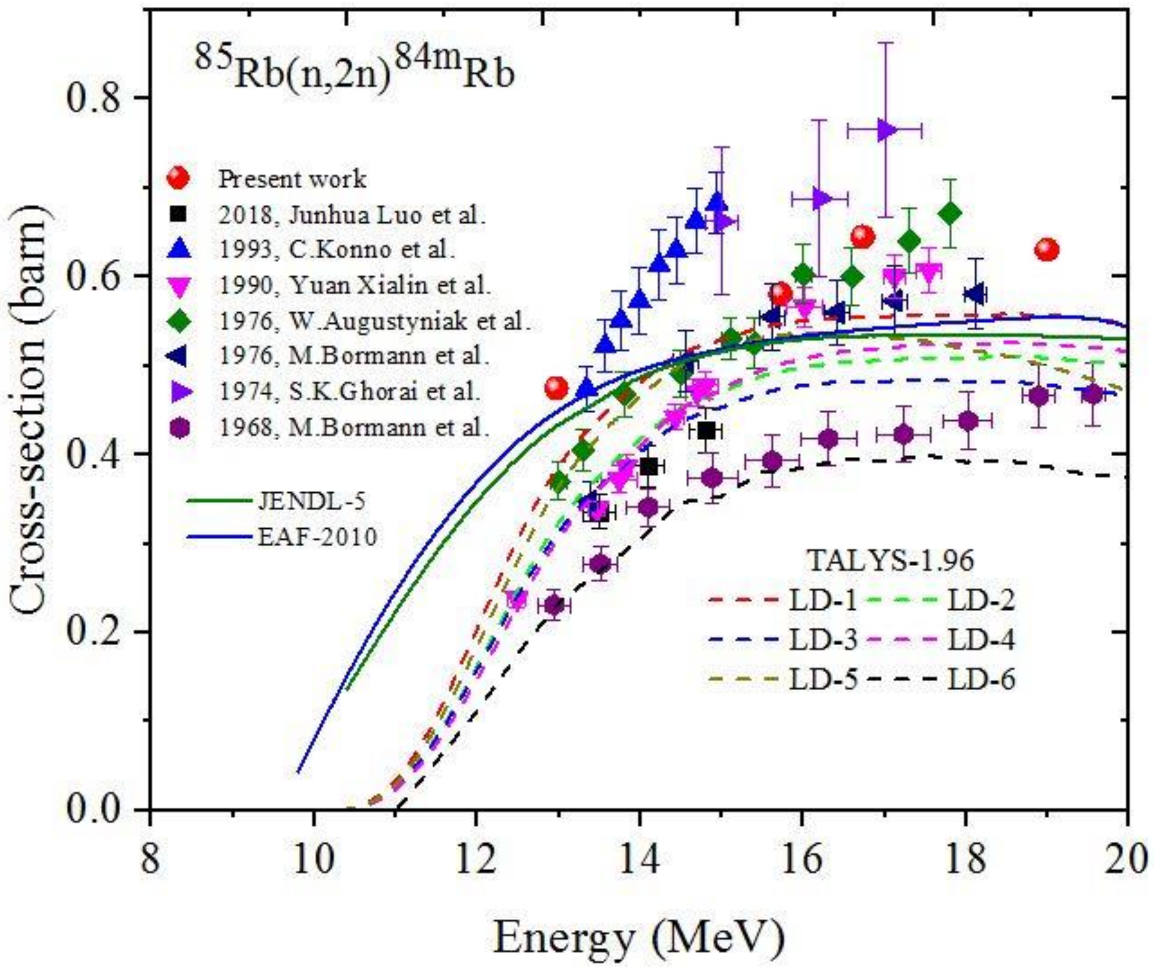

Figure 5.19 Comparison of ^{85}Rb(n,2n)^{84m}Rb reaction cross section with reported data, theoretically calculated data by TALYS-1.96 and evaluated data

5.4.3 Results and Discussion

Tables 5.33 and *5.35* represent the ^{85}Rb(n,p)^{85m}Kr and ^{85}Rb(n,2n)^{84m}Rb reaction cross sections with uncertainties and correlation matrix. It is observed that there is less than 8% of overall uncertainty in the measured cross sections for both reactions. *Figure 5.18* shows the comparison between the measured ^{85}Rb(n,p)^{85m}Kr reaction cross section and the evaluated data [16–17], reported data [109–117], and theoretically predicted data from TALYS-1.96 [8]. The closest energy point values were taken into consideration when comparing the findings of the measured cross sections with the available data. According to the comparative results, the cross section accords with the ldmodel 2 and ldmodel 3 at 12.97 ± 0.51 MeV, the JENDL-5 at 15.72

± 0.60 MeV, and the ldmodel 4 at 16.73 ± 0.66 MeV, respectively. At 18.99 ± 0.74 MeV the result is agreed with the reported data by M. Bormann et al. [114] at 18.89 MeV (0.003 barns).

Similarly, the comparison of the measured ^{85}Rb(n,2n)^{84m}Kr reaction cross section with the reported data [115-123], evaluated data [16-17] and theoretically predicted data from TALYS-1.96 [74] are plotted in *Figure 5.19*. For the ^{85}Rb(n,2n)^{84m}Rb reaction, the cross section values are overestimate with the evaluated data and theoretically predicted data by TALYS 1.96. The cross section values at 12.97 ± 0.51 MeV and 18.99 ± 0.74 MeV are overestimated with the reported data by M. Bormann et al. [120] at 12.94 MeV (0.231 barns) and 18.89 MeV (0.466 barns), respectively. The cross section results at 15.72 ± 0.60 MeV and 16.73 ± 0.66 MeV are consistent within 10% with the reported data by W. Augustyniak et al. [126] at 15.4 MeV (0.525 barns) and 16.6 MeV (0.6 barns), respectively. In case of ^{85}Rb(n,2n)^{84m}Rb reaction, 463.62 (33.1%) keV γ-ray energy was used for the cross section measurements which was earlier used by S.K. Ghorai et al. [121] and B. Minetti et al. [123] earlier. The comparison of measured values at 15.72 ± 0.60 MeV and 16.73 ± 0.66 MeV indicate that the values are agreed within 12% and 6% to the reported values by S.K. Ghorai et al. [121] at nearest energy points at 15 MeV (0.662 barns) and 16.2 MeV (0.688 barns).

5.6 Conclusion

The ^{90}Zr(n,2n)^{89}Zr, ^{90}Zr(n,p)^{90m}Y, ^{93}Nb(n,2n)^{92m}Nb, ^{88}Sr(n,2n)^{87m}Sr, ^{85}Rb(n,2n)^{84m}Rb and ^{85}Rb(n,p)^{85m}Kr reactions cross sections were determined using the neutron activation and offline γ-ray spectrometry technique in the neutron energy range of 10 to 20 MeV. The associated *Tables* provide the results of the reactions cross section, including uncertainty, covariance, and correlation matrix. All the measured cross section values were compared with the evaluated data, theoretically predicted data using TALYS and EMPIRE programs, and data from the literature that was readily available through the EXFOR database.

The ^{90}Zr(n,2n)^{89}Zr and ^{90}Zr(n,p)^{90m}Y reactions

At average neutron energies of 13.97 ± 0.68 and 16.99 ± 0.53 MeV, the ^{90}Zr(n,2n)^{89}Zr reaction cross section agree with the previously published data. In a similar vein, the ^{90}Zr(n,p)^{90m}Y reaction cross section at neutron energies of 10.95 ± 0.45, 16.99 ± 0.53, and 20.02 ± 0.58 MeV agrees with previously published data. In the neutron energy range of 16-22 MeV, there are some differences in the literature data for both the reactions, though the goal of this work is to improve and close the gaps in the IAEA-EXFOR database in this range of neutron energies. For the ^{90}Zr(n,2n)^{89}Zr and ^{90}Zr(n,p)^{90m}Y reactions, theoretical predictions made with the TALYS-1.9 and EMPIRE-3.2.2 codes with optimal input parameters from threshold to 22 MeV accorded well with the current findings and data that has been previously published.

The ^{93}Nb(n,2n)^{92m}Nb, ^{88}Sr(n,2n)^{87m}Sr reactions

Using the activation and offline γ-ray spectroscopy approach, the (n,2n) reaction cross sections of the ^{92m}Nb and ^{87m}Sr isotopes were estimated in the neutron energy range of 13.97 MeV to 20.02 MeV. The current data for ^{93}Nb(n,2n)^{92m}Nb reaction cross sections differ by approximately 12% from the previously measured values at 13.97 MeV energy by Wang Xiuyuan et al. and by approximately 30% at 20.02 ± 0.58 MeV. The difference is roughly 10% for the ^{88}Sr(n,2n)^{87m}Sr reaction between the current data and the previously published data around 13.9 MeV by C. Konno et al. and between 3%- 9% for the previously published data by M. Bormann et al. There are few cross section measurements available from threshold to 18 MeV neutron energies with significant variations. The cross section data for both reactions is lacking, so future study will concentrate on accurately conducting experiments in this energy band to enhance nuclear data base.

The ^{85}Rb(n,p)^{85m}Kr and ^{85}Rb(n,2n)^{84m}Rb reactions

The ^{85}Rb(n,p)^{85m}Kr and ^{85}Rb(n,2n)^{84m}Rb reactions cross sections were determined in the energy range from 12 to 20 MeV using the offline γ-ray spectroscopic method. The absolute neutron flux was determined using ^{27}Al(n,α)^{24}Na monitor reaction. The cross section values for both reactions were compared with the data reported in the literature, theoretical calculations using TALYS-1.96 and evaluated data from JENDL-5 and EAF-2010. Multiple data points with scarcity in measured values are seen for both the reactions. The reason is due to using different reference monitor cross section by authors. For ^{85}Rb(n,p)^{85m}Kr reaction, the measured value has a slightly increasing trend with the increase in neutron energy indicating that the high-spin isomer formation is more favored at higher excitation energies. For ^{85}Rb(n,2n)^{84m}Rb reaction, the measured values at 15.72 and 16.73 MeV energies were aligned with the reported values while at 12.97 MeV and 18.99 MeV, the measured values were overestimated with the reported values. The cross section values in the present work were reported with the detailed uncertainties, covariance and correlation matrix. The measured data will fill up the gap at the neutron energies where there is a deficiency in the cross section data.

References

---

[1] Mayur Mehta, N. L. Singh, R. K. Singh, Siddharth Parashari, P. V. Subhash, H. Naik, R. D. Chauhan, R. Makwana, S. V. Suryanarayana, S. Mukherjee, A. Gandhi, J. Varmuza And K. Katovsky, J. of Radioanalytical and Nuclear Chemistry, 328 (2021) 71

[2] Mayur Mehta, N. L. Singh, Ratankumar Singh, Rakesh Chauhan, Rajnikant Makwana, S. V. Suryanarayana, H. Naik, P. V. Subhash, S. Mukherjee, Jan Varmuza, Karel Katovsky, *Applied Radiation and Isotopes 182 (2022) 110142*

[3] Mayur Mehta, N. L. Singh, Ratankumar Singh, Rajnikant Makwana, P. V. Subhash, Rakesh Chauhan, Bhargav Soni, S. V. Suryanarayana, H. Naik, R. Palit, Karel Katovsky, in review in Nuclear Physics Section A.

[4] C. H. Poppe, J. D. Anderson, J. C. Davis et al., Phys. Rev. C 14 (1976) 438.

[5] S. G. Mashnik, M. B. Chadwick, H. G. Hughes et al., Los Alamos National Laboratory, Los Alamos, NM 87545, USA (2008), arXiv:nucl-th/0011066v1

[6] N. Otuka, B. Lalremruata, M.U. Khandaker, A.R. Usmand, L.R.M. Punte, Radiation Physics Chemistry 140 (2017) 502-510.

[7] EXFOR, Experimental Nuclear Reaction Data, http://www-nds.iaea.org/exfor

[8] A. J. Koning, TALYS-1.9, A Nuclear reaction program, user’s manual, NRG-1755 ZG Petten, The Netherlands (2018).

[9] M. Herman et al., Nucl. Data Sheets, 108 (2007) 2655.

[10] M. Herman, A. Trkov, Nucl Data Sheets 148 (2018) 214-253.

[11] K. Shibata, O. Iwamoto, T. Nakagawa, et al., J. Nucl. Sci. Technol. 48 (2011) 1-30.

[12] A. J. Koning, E. Bauge, C. J. Dean et al., J. Korean Phys. Soc. 59 (2011) 1057-1062.

[13] S. V. Zabrodskaya, A. V. Ignatyuk, V. N. Koscheev, Nuclear constants, ROSFOND-2010 (2007) 1-2.

[14] K. Shibata, N. Iwamoto, S. Kunieda, F. Minato, O. Iwamoto, Activation cross section File for Decommissioning of LWRs, JAEA Conf. 2016-004, 47-52.

[15] A. J. Koning, D. Rochman, J. Sublet, N. Dzysiuk, M. Fleming and S. van der Marck, Nuclear Data Sheets 155 (20190 1.

[16] O. Iwamoto, N. Iwamoto, S. Kunieda, F. Minato, S. Nakayama, Y. Abe et al., J. Nucl. Sci. Technol. 60(1) (2023) 1-60.

[17] L.W. Packer and J-Ch. Sublet, The European Activation File: EAF 2010 decay data library, CCFE-R (10)02 (2010).

[18] BARC-TIFR Pelletron LINAC Facility at TIFR, Mumbai, http://www.tifr.res.in

[19] J. F. Ziegler, Nucl. Instrum. Methods in Physics Research Section B 219-220 (2004) 1027-1036.

[20] S. Parashari, S. Mukherjee, S. Suryanarayana et al., European Physics Journal A 55 (2019) 1-16.

[21] M. W. Mcnaughton, N. S. P. King, F. P. Brady et al., Nuclear Instrumentation and Methods 130 (1975) 555-557.

[22] Bhargav Soni, Siddharth Parashari, S. Mukherjee et al., Eur. Phys. J. Plus, 135 (2020) 300.

[23] Siddharth Parashari, S. Mukherjee, S. V. Suryanarayana et al., Phys. Rev. C 99 (2019) 044602.

[24] Siddharth Parashari, S. Mukherjee, H. Naik et al., Eur. Phys. J.A. 55 (2019) 51.

[25] Rajnikant Makwana, S. Mukherjee, P. Mishra, et al., Phys. Rev. C 96 (2017) 024608.

[26] D. L. Smith et al., Corrections for Low Energy Neutrons by Spectral Indexing, retrieved from, https://www.oecdnea.org/science/docs/2005/nsc-wpec-doc2005-357.pdf

[27] R. Krishnan and M. K. Asundi, Proc. Indian Aead. Sci. (Engg. Sei.), 4 (1980) 41-56.

[28] Clement Lemaignan, Arthur T. Motta, Materials Science and Technology, (15 September 2006) 4-47.

[29] Michal Kostal, Martin Schulc, Vojtech Rypar et al., Applied Radiation and Isotopes 128 (2017) 92-100.

[30] M. S. Uddin, M. U. Khandaker, K. S. Kim et al., Nucl. Instr. Methods Phys. Res. B, 266 (2008) 13-20.

[31] R. A. Forrest, Fusion Eng. Design, 81 (2006) 2143.

[32] G. Aliberti, G. Palmiotti, M. Salvatores, Ann. Nucl. Energy 33 (2006) 700.

[33] J. A. Shusterman, N. D. Scielzo, K. J. Thomas et al., Nature 565 (2019) 328-330.

[34] NuDat 2.8 (2020) National Nuclear Data Center, Brookhaven National Laboratory. http://www.nndc.bnl.gov/nudat2

[35] Calculation of Reaction Q-Values and Thresholds, Los Alamos National Laboratory, T-2 Nuclear Information Service, from http://www.nndc.bnl.gov/qcalc/ retrieved 8th May 2020

[36] R. B. Firestone, Nuclear Data Sheets, 108 (11) (2007) 2319-2392.

[37] Jean Blachot, Nuclear Data Sheets 113 (10) (2012) 2391-2535.

[38] B. Singh, Nuclear Data Sheets 114 (1) (2013) 1-208.

[39] E. Browne, Nuclear Data Sheets 82(3) (1997) 379-546.

[40] M. J. Martin, Nucl Data Sheets, 114, 1497-1847 (2013)

[41] J. J. Griffin, Phys. Rev. Lett., 17 (1966) 478.

[42] T. Vidmar, Nuclear Instruments Methods A 550 (2005) 603

[43] T. Vidmar, G. Kanisch, G. Vidmar, Applied Radiation and Isotopes 908 (2011) 69.

[44] S. Parashari, S. Mukherjee, S. Suryanarayana et al., European Physics Journal A 55 (2019) 1-16.

[45] A. J. Koning and D. Rochman, Nuclear Data Sheets 113 (12) (2012) 2841-2934.

[46] R. Capote, M. Herman, P. Oblozinsky, et al., Nucl Data Sheets 110 (2009) 3107.

[47] A. J. Koning, J. P. Delaroche, Nucl. Phys. A 713 (2003) 231.

[48] W. Hauser and H. Feshbach, Phys. Rev. 87 (1952) 366.

[49] A. J. Koning, M. C. Duijvestijn, Nucl Phys A., International Conference on Nuclear Data for Science and Technology (2007) 211-214.

[50] A. Gilbert, A. G. W. Cameron, Can. J. Phys. 43 (1965) 1446.

[51] W. Dilg, W. Schantl, H. Vonach, M. Uhl, Nucl. Phys. A 217 (1973) 269.

[52] A. V. Ignatyuk, K. K. Istekov, G. N. Smirenkin, Sov. J. Nucl. Phys. 29 (1979) 450.

[53] A. V. Ignatyuk, J. L. Weil, S. Raman, S. Kahane, Phys. Rev. C 47 (1993) 1504.

[54] S. Goriely, S. Hilaire, A.J. Koning, Phys. Rev. C 78 (2008) 064307.

[55] S. Hilaire, M. Girod, S. Goriely, A. J. Koning, Phys. Rev. C 86 (2012) 064317.

[56] A. Gandhi et al., Journal of Radioanalytical and Nuclear Chemistry 322 (2019) 89.

[57] A. Kalamara, et al., The European Physical Journal A 55 (2019) 187.

[58] J. Raynal, IAEA unpublished, SMR-9/8. 28

[59] J. Raynal, Computing as a language of physics, in ICTP International Seminar Course, Trieste, Italy (IAEA, 1972) 281.

[60] B. Morillon and P. Romain, Phys. Rev. C 76 (2007) 044601.

[61] H. M. Hofmann et al., Ann. Phys. 90 (1975) 403.

[62] V. A. Plujko, Acta Phys. Pol. B 31 (2000) 435.

[63] J. J. Griffin, Phys. Rev. Lett., 17, 478 (1966)

[64] A. A. Filatenkov, Neutron activation cross sections measured at KRI in neutron energy region 13.4 - 14.9 MeV, Report: USSR report to the I.N.D.C.No.0460, 2016

[65] V. Semkova, E. Bauge, A.J.M. Plompen, et al., Nuclear Physics A 832 (2010) 149.

[66] Qiu Jiuzi, Yuan Junqian, Yang Jingkang, Journal of Lanzhou Univ., Natural Science Ed., 32 (1997) 57.

[67] A. Pavlik, G. Winkler, H. Vonach, et al., Jour. of Physics, Part G (Nucl. and Part. Phys.) 8 (1982) 1283.

[68] Y. Kanda, Nuclear Physics A, 185 (1972) 177.

[69] Zhao Wenrong, Lu Hanlin, Fan Peiguo, Chinese J. of Nuclear Physics (Beijing), 6(1) (1984) 80.

[70] N. I. Molla, R. U. Miah, M. Rahman, et al., Conf. on Nucl. Data for Sci. and Technol., Juelich (1991) 355.

[71] Y. Ikeda, C. Konno, K. Oishi, et al., Report: JAERI Reports No.1312 (1988).

[72] Y. Ikeda, H. Maekawa, T. Nakamura, et al., Radiation Effects 92 (1986) 175.

[73] B. P. Bayhurst, J. S. Gilmore, R. J. Prestwood, et al., Physical Review C 1 (1975) 451.

[74] A. Abboud, P. Decowski, W. Grochulski, et al., Nuclear Physics A 139 (1969) 42.

[75] P. Raics, S. Nagy, S. Szegedi, N.V. Kornilov, A.B. Kagalenko, Conf. on Nucl. Data for Sci. and Technol., (Juelich 1991) 660.

[76] A. Marcinkowski, U. Garuska, H.M. Hoang, et al., Nuclear Physics A 510 (1990) 93.

[77] M. IbnMajah, A. Chiadli, S. Sudar, et al., Applied Radiation and Isotopes 54 (2001) 655.

[78] R. Doczi, V. Semkova, A. Fenyvesi, et al., Nuclear Science and Engineering 129 (1998) 164.

[79] M. IbnMajah, S. M. Qaim, Nuclear Science and Engineering, 104 (1990) 271.

[80] P. M. Prajapati, S. Mukherjee, H. Naik, et al., Nuclear Science and Engineering 171 (2012) 78.

[81] Imran Pasha, Rudraswamy Basavanna, et al., Journal of Radioanalytical and Nuclear Chemistry 320 (2019) 561-568.

[82] M. Majerle, P. Bem, J. Novak, E. Simeckova, et al., Nuclear Physics, Section A 953 (2016)139.

[83] M. Honusek, P. Bem, V. Burjan, et al., Journal of the Korean Physical Society 59 (2011)1374.

[84] Y. Uno, S. Meigo, S. Chiba, T. Fukahori, et al., Measurements of activation cross sections for the neutron dosimetry at an energy range from 17.5 to30 MeV by using the ^{7}Li(p,n) quasi-mono-energetic neutron source, Conf.: 9th Internat. Symposium on Reactor Dosimetry, Prague (1996) 465.

[85] A. Fessler, et al., Nuclear Science and Engineering, 134 (2) (2000) 171.

[86] Zhao Wenrong, et al., Compilation of measurements and evaluations of nuclear activation cross sections for nuclear data application, Report: Chinese report to the I.N.D.C.No.16, 1989.

[87] D. C. Santry, R. D. Werner, Canadian Journal of Physics, 68 (1990) 582.

[88] A. A. Filatenkov, Neutron activation cross sections measured at KRI in neutron energy region 13.4-14.9 MeV, Report: USSR report to the I.N.D.C.No.0460, 2016.

[89] He. Guozhu, et al., Annals of Nuclear Energy 33 (2006) 37.

[90] C. Konno, Activation Cross section measurements at neutron energy from 13.3 to 14.9 MeV, Report: JAERI Reports No.1329, 1993.

[91] M. Bormann, et al., Zeitschriftfuer Physik A, Hadrons and Nuclei, 277 (1976) 203.

[92] M. Bormann, Nuclear Physics, 63 (1965) 438.

[93] C.V. Srinivasa Rao, et al., Fluctuations in the systematics of (n,2n) reaction cross sections in the low mass region; Fast neutron cross sections of fusion reactor interest, Conf.: 21. Nucl. Phys. and Solid State Phys. Symp-1978., Bombay Vol.2 (1978) 113.

[94] B. Minetti, A. Pasquarelli, Nuclear Physics Section A 118 (1968) 449.

[95] N. I. Molla, Measurement of cross section for neutron induced reactions at 14 MeV via activation technique, Prog. Rep.: Bangladesh report to the I.N.D.C.No.002, 1983, pp.1.

[96] G. N Salaita, P. K. Eapen, Production of Isomers by the Cyclic Activation Method, Conf. on Nucl.Meth.in Envir. Res., Columbia-1974, 95.

[97] M. Hyvoenen-Dabek, Tarvainen, P. Holmberg, Journal of Radioanalytical Chemistry 46 (1978) 357.

[98] Coral M. Baglin, Nuclear Data Sheets 113(10) (2012) 2187-2389.

[99] T. D. Johnson, W. D. Kulp, Nuclear Data Sheets 129 (2015) 1-190.

[100] R. Nowotny, XMuDat: photo attenuation data on PC, IAEA Report No. IAEA-NDS 195 (1998).

[101] A. Trkov, P.J. Griffin, S.P. Simakov et al., Special issue of Nuclear Data Sheets 163 (2020) 1-108.

[102] M. Bostan, Phys. Rev. C 49 (1994) 266.

[103] K. Heyde, J.L. Wood, Rev. Mod. Phys. 83 (2011) 1467.

[104] A. Trkov, P.J. Griffin, S.P. Simakov et al., Special issue of Nuclear Data Sheets 163 (2020) 1-108.

[105] Daniel Abriola et al., Nuclear Data Sheets 110 (2009) 2815-2944.

[106] Balraj Singh and Jun Chen, Nuclear Data Sheets 116 (2014) 1-162.

[107] NuDat 3 (2023) National Nuclear Data Center, Brookhaven National Laboratory. http://www.nndc.bnl.gov/nudat3

[108] R. K. Singh, N. L. Singh et al., Chinese Physics C 46 (5) (2022) 054002.

[109] C. Konno, Y. Ikeda, K. Oishi, K. Kawade, H. Yamamoto, H. Maekawa Activation Cross section measurements at neutron energy from 13.3 to 14.9 MeV Report: JAERI Reports No.1329, 1993.

[110] R. Pepelnik, B. Anders, B.M. Bahal, M. Farooq, 14 MeV neutron activation cross sections-, Report: Ges.Kernen.-Verwertung, Schiffbau and Schiffahrt No.86-E-29, (1986).

[111] B. Erlandsson, A. Marcinkowski, K. Nilson, Physica Scripta 19 (3) (1979) 251.

[112] N.I. Molla, S.M. Qaim, Nuclear Physics, Section A 283 (1977) 269.

[113] L. Husain, A. Bari, P.K. Kuroda, Physical Review C, Nuclear Physics 1 (1970) 1233.

[114] M. Bormann, F. Dreyer, H. Neuert, I. Riehle, U. Zielinski, Measurements of some fast neutron cross sections with the activation method, Nuclear Data For Reactors Conf., Paris 1966 Vol.1 (196) 225.

[115] Yuan Xialin, Zhao Wenrong, Yu Weixiang, Lu Hanlin, Chinese J. of Nuclear Physics (Beijing), 12 (4) (1990) 289.

[116] W. Augustyniak, M. Herman, A. Marcinkowski, Acta Physica Polonica, Part B 7 (1976) 347.

[117] P. Venugopala Rao, R.E. Wood, J.M. Palms, R.W. Fink, Physical Review C, Nuclear Physics 3 (1971) 629.

[118] Junhua Luo, Li Jiang, Long He, Radiochimica Acta, 106(9) (2018) 709-717.

[119] C. Konno, Y. Ikeda, K. Oishi, K. Kawade, H. Yamamoto, H. Maekawa, Activation Cross section measurements at neutron energy from 13.3 to 14.9 MeV, Report: JAERI Reports No.1329 (1993).

[120] M. Bormann, H-K. Feddersen, H.-H. Holscher, W. Scobel, H. Wagner, Zeitschrift fuer Physik A, Hadrons and Nuclei 277 (1976) 203.

[121] S.K. Ghorai, R. Vos, J.R. Cooper, W.L. Alford, The (n,2n) cross sections of 85Rb, 87Rb and 144Sm, Nuclear Physics, Section A 223 (1974) 118.

[122] M. Bormann, A. Behrend, I. Riehle, O. Vogel, Nuclear Physics, Section A 115 (1968) 309.

[123] B. Minetti, A. Pasquarelli, Nuclear Physics Section A 118 (1968) 449.